



Deposited via The University of Leeds.

White Rose Research Online URL for this paper:

<https://eprints.whiterose.ac.uk/id/eprint/201342/>

Version: Accepted Version

Article:

Pang, X., Wang, G., Mountney, N.P. et al. (2023) Prediction of lamina structure and reservoir quality in shale using well logs: The Cretaceous Qingshankou Formation, Gulong Sag, Songliao Basin, China. *Geoenergy Science and Engineering*, 227. 211827. ISSN: 2949-8929

<https://doi.org/10.1016/j.geoen.2023.211827>

© 2023, Elsevier. This manuscript version is made available under the CC-BY-NC-ND 4.0 license <http://creativecommons.org/licenses/by-nc-nd/4.0/>. This is an author produced version of an article published in *Geoenergy Science and Engineering*. Uploaded in accordance with the publisher's self-archiving policy.

Reuse

This article is distributed under the terms of the Creative Commons Attribution-NonCommercial-NoDerivs (CC BY-NC-ND) licence. This licence only allows you to download this work and share it with others as long as you credit the authors, but you can't change the article in any way or use it commercially. More information and the full terms of the licence here: <https://creativecommons.org/licenses/>

Takedown

If you consider content in White Rose Research Online to be in breach of UK law, please notify us by emailing eprints@whiterose.ac.uk including the URL of the record and the reason for the withdrawal request.

1 **Prediction of lamina structure and reservoir quality in shale**
2 **using well logs: the Cretaceous Qingshankou Formation,**
3 **Gulong Sag, Songliao Basin, China**

4
5 Xiaojiao Pang^{1,2}, Guiwen Wang^{1,2}, Nigel P. Mountney³, Lichun Kuang^{1,2}, Xin Zhao^{1,2}, Yidi
6 Zhao^{1,2}, Hongbin Li^{1,2}, Zongyan Han^{1,2}, Han Tian²

7
8 1. State Key Laboratory of Petroleum Resources and Prospecting, China University of
9 Petroleum (Beijing), Beijing 102249, China

10 2. College of Geosciences, China University of Petroleum (Beijing), Beijing, 102249, China

11 3. School of Earth and Environment, Institute of Applied Geophysics, University of Leeds,
12 Woodhouse, Leeds, LS2 9JT

13 **Corresponding author:** Xiaojiao Pang, China University of Petroleum (Beijing), 18 Fuxue
14 Road, Changping, Beijing China 102249. E-mail: xiaojiaopang0829@163.com

15 Prof. Guiwen Wang, China University of Petroleum (Beijing), 18 Fuxue Road, Changping,
16 Beijing China 102249. Tel.: +861089733435; Fax.: +861089734158; E-mail:
17 wanggw@cup.edu.cn

18 **Abstract**

19 Lamina structure is determined by composition, thickness, continuity, and mineral assemblage.
20 Reservoir quality in oil shale reservoirs is determined by lamina structure, which controls
21 hydrocarbon accumulation and migration. The prediction and evaluation of multi-scale lamina
22 structures using geophysical well logs is challenging. Recent studies demonstrate that the

23 lamina structure classification may be based on core observation and core analysis. However,
24 there are no corresponding high-resolution geophysical logging methods to identify and
25 categorize lamina structure continuously in a single well. Here, an experimental approach,
26 involving an integrated analysis of cores, thin sections, well logs such as slabs and button
27 conductivity curves of image logs (up to 5 mm vertical resolution), is used to characterize
28 lamina structure. T_1 - T_2 (T_1 , longitudinal relaxation time, and T_2 , transverse relaxation time)
29 maps of nuclear magnetic resonance (NMR) logs is applied to clarify the relationships between
30 the lamina structure, reservoir quality, and oil-bearing properties. Results demonstrate how
31 lamina structure in shale can be divided into three types: laminated rocks, layered rocks, and
32 massive rocks, according to observation of core at the lamina scale. The thickness of individual
33 lamina is less than 0.01 m in the laminated rocks, and the layered rocks have bundles of
34 genetically related laminae thickness ranging between 0.01 m—0.1 m. In massive rocks there
35 is no visible layering. The well log response patterns of the three types of lamina structure are
36 established so that the distribution of lamina structure can be predicted in a single well via well
37 logs. Results show that the oil-bearing shale intervals are dominated by laminated rocks and
38 layered rocks, accounting for 90% of the studied Qingshankou Formation. In addition, the
39 layered rocks play an important role in improving reservoir quality and the laminated rocks
40 present moderate reservoir quality. The massive rocks show poor reservoir quality. Moreover,
41 an increased proportion of felsic mineral content favors increased oil potential in oil shale
42 reservoirs. The method is generally applicable and is of value in developing predictive
43 indicators of subsurface reservoir sweet spots in shale oil and gas exploration and development.
44 **Key words:** Shale oil; lamina structure; reservoir quality; image logs; T_1 - T_2 map

45

46 **1. Introduction**

47 Recently, unconventional reservoirs have become a focus of exploration and development,
48 [\(Zou et al., 2013; Newport et al., 2016; Soeder., 2017; Yang et al., 2019\)](#). Oil shale reservoirs
49 are distributed worldwide. Examples from the USA include the Bakken shale in the Williston
50 Basin [\(Saidian and Prasad., 2015\)](#), the Eagle Ford shale in southern Texas [\(Ko et al., 2017\)](#), and
51 the Barnett shale in the Fort Worth Basin [\(Jarvie et al., 2007; Hill et al., 2007; Loucks et al.,](#)
52 [2009\)](#). Examples from China include the Triassic Yanchang Formation in the Ordos Basin, the
53 Cretaceous Qingshankou Formation in the Songliao Basin [\(Lin et al., 2021\)](#), the Jurassic
54 Longmaxi Formation in Sichuan Basin [\(Tang et al., 2019\)](#), the Paleogene Kongdian Formation
55 in the Bohai Bay Basin [\(Yang et al., 2019\)](#) and the Permian Lucaogou Formation in the Junggar
56 Basin [\(Pang et al., 2022\)](#). The proportion of shale oil and gas has increased steadily since the
57 “shale revolution”, indicating an important resource prospect in the future [\(Hou et al., 2021\)](#).
58 In addition, established technologies – including horizontal well drilling, volume fracturing
59 stimulation, and refracturing – make it possible to produce oil and gas from shales, in addition
60 to from coarser-grain clastic sandstone reservoirs using conventional production techniques
61 [\(Zou et al., 2017; Yang et al., 2019\)](#). However, the energy industry is facing technical challenges
62 in terms of drilling, exploration, development, and production of unconventional resources.
63 They are more difficult to extract because production typically requires fracturing the rock
64 formation to allow resources to accumulate in sufficient quantities and flow from the well. The
65 occurrence of laminae (bedding) and lamellation fractures determine reservoir quality and
66 engineering quality in sales – described by paramters including, for example, brittleness index,

67 in situ stress, and fracability. Laminae can change into bedding parallel fractures during burial,
68 where subject to diagenesis and compaction. This may be helpful for oil and gas accumulation
69 since it favors improved fracture network formation during the later fracturing (Lai et al.,
70 2022a). It is important to investigate the controlling relationships of laminae and lamellation
71 fractures upon reservoir quality and oil-bearing properties. Moreover, the characterization of
72 multi-scale laminae can be obtained through a variety of observation methods and well log
73 technologies; for example, the direct observation of cores, thin sections and scanning electron
74 microscopy (SEM) photomicrographs, and the interpretation of conventional geophysical logs
75 using long-established techniques (Weidlich et al., 2004; Xavier and Fagel., 2005; Chen et al.,
76 2017; Li et al., 2020; Wang et al., 2021). Decimeter- to meter-scale bundles of genetically
77 related laminae have been characterized using well log tools, including gamma-ray logs, deep
78 and low resistivity logs, three porosity logs (density, neutron, and sonic interval transit time
79 logs), and image logs (Wang et al., 2021; Lai et al., 2022b). However, there are no
80 comprehensive logging evaluation methods for lamina structure and the relevant reservoir
81 quality and oil-bearing properties controlled by small-scale lamina structure in oil shale
82 reservoirs.

83 As a contribution to the worldwide growth in production and exploration of
84 unconventional oil and gas, oil shale reservoirs have been discovered in the Upper Cretaceous
85 Qingshankou and Nenjiang formations of the Gulong Sag, Songliao Basin, China (Bechtel et
86 al., 2012; Xu et al., 2015). The Cretaceous Qingshankou Formation shale contains notable shale
87 oil resources. Over the past two decades, high-resolution studies of the potential for
88 hydrocarbon generation, the reconstruction of paleoenvironmental changes, the organic

89 geochemistry, mineralogy, lithology, and lithofacies have been undertaken (Zhou and Littke,
90 1999; Xu et al., 2015; Liu et al., 2019; Sun et al., 2021). The shale reservoir in the Qingshankou
91 Formation is characterized by self-generation and self-containment in the lacustrine source
92 rocks (Li et al., 2017; Cui et al., 2020; Lin et al., 2021). There has been no migration (including
93 micron-nano migration) identified; the hydrocarbon generation has not commenced expulsion
94 because the limit of capillary resistance pressure, viscosity force, and friction force have not
95 yet been exceeded (Feng et al., 2020). The reservoir is highly heterogeneous and characterized
96 by complex sedimentary characteristics (Li et al., 2019; Yang et al., 2019; Hou et al., 2021).
97 Notably, the presence of abundant laminae and bedding-parallel fractures differentiate this
98 formation from other shale reservoirs developed in lacustrine palaeo-depositional environments
99 (Li et al., 2019). These features are considered to be the key factors controlling the potential
100 production of shale oil (Drager et al., 2016; Liu et al., 2019; Lai et al., 2022a). Therefore, it is
101 essential to determine the role of the lamina structure in controls reservoir properties.

102 The aim of this study is to classify shale lamina structure, establish a logging evaluation
103 method of multi-scale lamina structure, and assess their impact on reservoir quality. The
104 reservoir characteristics of mineral composition, laminae types, lamina structure, and porosity
105 are described through the core photos, XRD, and porosity experiment. The multi-scale lamina
106 structure is identified by advanced well-log analysis, especially using image logs (slabs and
107 button conductivity curves). These techniques are used to identify the millimeter- to meter-scale
108 bundles of genetically related laminae according to their high resolution (5 mm). This allows
109 for the lamina structure to be determined in a single well. T₁-T₂ maps of single and stacked
110 depth derived from 2D NMR logs are used to characterize the reservoir quality and oil-bearing

111 properties. This study provides essential insights into the quality and oil-bearing properties of
112 a shale reservoir. The results can provide guidance for shale oil and gas exploration and
113 development more widely.

114

115 **2. Geological setting**

116 The Songliao Basin is a significant and petroliferous basin in northwestern China, which
117 spans three provinces, including Heilongjiang, Jilin, Liaoning, and Inner Mongolia; it covers
118 more than 287,000 km² (Ge et al., 2010; Li et al., 2021a). The basin is divided into six tectonic
119 units: the southwestern slope zone, southwestern uplift zone, northern uplift zone, central
120 depression zone, northeastern uplift zone, and southeastern uplift zone (Fig. 1) (Li et al., 2021;
121 Lin et al., 2021). Different sedimentary facies accumulated in the different tectonic zones: for
122 example, alluvial-fan and fan-delta successions are located adjacent to steep basin-margin
123 slopes, whereas braided rivers deltas developed across gently inclined slopes (Ge et al., 2010).
124 A semi-deep to the deep lake (lacustrine) succession was accumulated in the depression zones
125 (Ge et al., 2010).

126 The Gulong Sag is located in the western central depression zone of the northern basin; it
127 covers an area of 3,700 km² (Chen et al., 2013; Li et al., 2021). Early Cretaceous strata in
128 Gulong Sag can be divided into four formations: Shahezi Formation, Yingcheng Formation,
129 Denglouku Formation, and Quantou Formation, from the bottom to the top (Li et al., 2017;
130 Feng et al., 2020; Li et al., 2021). Additionally, late Cretaceous strata consist of the
131 Qingshankou Formation, Yaojia Formation, Nenjiang Formation, Sifangtai Formation, and
132 Mingshui Formation from the bottom to the top (Li et al., 2017; Feng et al., 2020; Li et al.,

133 2021). The Qingshankou Formation, which conformably overlies the Quantou Formation and
134 conformably underlies the Yaojia Formation, has abundant hydrocarbon resources and great
135 exploration and development potential in shale oil (Feng et al., 2020; Li et al., 2021).

136 The Qingshankou Formation is subdivided into two members. Member 1 of the
137 Qingshankou Formation covers an area of 4,200 km²; Member 2 covers an area of 2,800 km²,
138 and is deposited after Member 1 (Pang et al., 2021; Li et al., 2021). The main sedimentary facies
139 of the Qingshankou Formation were semi-deep to deep lakes that were rich in organic matter.
140 Member 1 accumulated during a development of a maximum flooding surface, contributing to
141 shale oil and gas accumulation (Li et al., 2020). In addition, the formation of organic pores and
142 bedding-parallel fractures attributed to the hydrocarbon generation evolution during the burial,
143 and thermal history were also essential for oil and gas accumulation and generation (Li et al.,
144 2020; Feng et al., 2020; Lai et al., 2021).

145

146 **3. Data and methods**

147 In our study, five key wells named Wells A, B, X, Y, and Z are selected to predict the oil
148 shale reservoir quality of the Cretaceous Qingshankou Formation, Gulong Sag, Songliao Basin
149 (Fig.1c). More than 1600 core photos taken from Well B and Well X were used to observe the
150 characteristics of lithologies and lamina structure of the Qingshankou Formation. Optical
151 microscopy and X-ray Diffraction (XRD) were used to complement mineral characterization,
152 identify types of pore space and observe oil-bearing properties. A total of 297 core samples
153 selected from Well X were prepared for XRD measurement using machine PANalytical X'Pert
154 Powder. These samples are roughly crushed to obtain various mineral types and contents using

155 a system containing an experimental machine and analytical software. Thin sections were
156 prepared according to a standard procedure, including freeze-drying and impregnation ([Brauer
157 and Casanova, 2001](#)). Twenty-one core samples selected from Well A were cut to a thickness
158 of 30 μm . They were mounted on slides ready for investigation under a microscope with both
159 non-polarized and polarized light. All tests were completed at the State Key Laboratory of
160 Petroleum Resources and Prospecting, China University of Petroleum Beijing. Petrophysical
161 parameters including total porosity and effective porosity were obtained to evaluate the
162 reservoir quality. The total porosity may be defined as all the pore space containing fluids (water,
163 oil or gas), whether or not they are mobile. There are various definitions of effective porosity.
164 In our study, effective porosity is defined as the ratio of interconnected pore volume to total
165 pore volume in rocks. Two-hundred-and-six samples in the Cretaceous Qingshankou Formation
166 in Well B have been analyzed using a Helium Porosity Instrument AP-121-003-1.

167 Wire-line log suites, comprising gamma-ray, array induction resistivity, and three porosity
168 logs (bulk density, neutron porosity, and sonic interval transit time) of all these five wells in
169 figure 1 were used to detect the meter scale bedding. Conventional well logs can only identify
170 decimeter- to meter-scale stratal packages.

171 Borehole images derived from Schlumberger's fullbore formation microimager (FMI) are
172 another effective source for detailed geological interpretation; these can be used to provide a
173 continuous image of the sub-surface geology, as seen in the borehole wall ([Kumar et al., 2014](#);
174 [Bize et al., 2015](#); [Lai et al., 2018](#)). Slabs derived from the image logs exhibit the planar surfaces,
175 such as bedding planes, fractures, faults, as straight lines, as seen in the core slabs rather than
176 the sinusoids typically seen on the borehole images ([Fig. 2](#)). Image logs are especially useful

177 and well-suited to the identification of the laminae, especially in oil shale reservoirs.
178 Appropriate image-log tools offer a high spatial resolution (up to 5 mm). Image logs can
179 recognize laminae and laminae bundles ranging from millimeter- to meter-scale. In our study,
180 image logs of three key wells (Wells X, Y, and Z) are available. Actually, the slab is the pseudo
181 image of the strata, which represents the electrical contrasts. The slab displays clearer bedding
182 characteristics than either the static or the dynamic images. When establishing the plate of well
183 log response of three types of lamina structure, core photos are used for log calibration. At
184 present, the identification of lamina type is undertaken manually, because no available and
185 precise automatic identification method has yet been established.

186 Conventional Nuclear Magnetic resonance (NMR) logs are commonly used to evaluate
187 the reservoir quality, including porosity and permeability, because only T_2 signals can be probed.
188 Two-Dimensional Nuclear Magnetic Resonance (2D NMR) logs are commonly used to test
189 both the longitudinal relaxation time (T_1) and the transverse relaxation time (T_2) of fluid-
190 saturated rocks (Li et al., 2018). Various parameters of physical properties can be derived from
191 NMR logs, including porosity, permeability, saturation, etc. The T_2 spectra profile, containing
192 the characterization of pore size distribution and fluid property, is profitable for evaluating
193 reservoir quality. Two-dimensional NMR maps (T_1 - T_2 maps) are obtained and these will be
194 used to exhibit the fluid types. These types consist of kerogen ($T_2 < 1$ ms, $T_1/T_2 > 100$), absorbed
195 oil (T_2 between 0.22 ms – 1 ms, T_1/T_2 between 25 – 100), free oil ($T_2 > 1$ ms, T_1/T_2 between 10
196 – 100), structural water ($T_2 < 0.22$ ms, $T_1/T_2 < 100$), absorbed water ($T_2 < 1$ ms, $T_1/T_2 < 10$),
197 free water (T_2 1 ms – 10 ms, $T_1/T_2 < 10$), bulk oil and bulk water according to the response of
198 each component in rocks (Li et al., 2018). The proton components can be effectively identified,

199 and the pore fluid types and distributions in shales can be calculated according to the cut off
200 values of T_2 and the ratio of T_1 to T_2 (Marc and Maria., 2016; Zhang et al., 2020). In addition,
201 continuous T_1 and T_2 data allow independent fluid volume and distribution assessment,
202 wettability comparisons, and quantification of asphaltene content. Collectively these
203 observations provide general information for petrophysical models as an alternative to using
204 conventional methods to evaluate oil and gas saturation (Zhang et al., 2020).

205 In this study, Combinable Magnetic Resonance logging (CMR-NG) was used to obtain
206 continuous T_1 and T_2 spectra; T_1 - T_2 maps were processed using Techlog 2019 Software. The
207 logging data are measured by the new generation of high-resolution NMR logs with the shortest
208 echo interval of 200 μ s and a low resonance frequency of 2 MHz in the low magnetism field,
209 which was developed by Schlumberger. Six groups of parameters were set. The wait times were
210 2s, 0.3s, 0.05s, 0.01s, 0.003s, and 0.0012s, respectively. The number of echoes were 1800, 600,
211 100, 50, 20, and 20. The repetition counts were 1, 2, 10, 30, 50 and 50. The Echo spacings were
212 0.2 ms, 0.2 ms, 0.2 ms, 0.2 ms, 0.28 ms and 0.28 ms. Two key wells (Well Y with a study-
213 interval thickness of 136.8 m) and Well Z (137.9 m) were examined to study shale deposits of
214 the Qingshankou Formation in terms of their reservoir quality and oil-bearing properties. The
215 quality control (QC) process is shown in figure 3. A spectrum of T_1 and T_2 can be obtained
216 every 190.5 mm (Fig. 4A); abundant nuclear magnetic resonance spectra data, therefore, are
217 available to characterize the reservoir quality and oil-bearing property. The T_1 and T_2 spectra
218 distribution and the T_1 - T_2 maps of single or stacked depth were obtained after NMR logs
219 processing through Software Techlog 2019 (Fig. 4B, 4C). Due to the lack of calibration of
220 laboratory data for 2D NMR, the T_2 and T_1/T_2 cut-offs relating to different fluid types cannot

221 be defined. Therefore, the oil-bearing property was qualitatively evaluated according to the
222 energy cluster position displayed in T₁-T₂ maps. The T₂ spectra are used to help characterize
223 the reservoir quality, and the T₁-T₂ maps provide insight into fluid properties (Xu et al., 2023).

224

225 **4. Results**

226 **4.1. Petrology characteristics**

227 [Figure 5](#) shows the mineralogical compositions of the shales in the Qingshankou
228 Formation of Gulong Sag. Insights through the XRD analysis, the dominant minerals consist of
229 terrigenous clastics, carbonates, and clay minerals. The contents of quartz, feldspar, calcite,
230 dolomite and clay mineral are 0.7–43.4%, 1.3–53.9%, 0–76.7%, 0–96.6%, and 0–79.0%,
231 respectively. The average contents of quartz, clay minerals, feldspar, dolomite, calcite, pyrite,
232 and siderite accounted for 30.7%, 29.6%, 21.3%, 8.9%, 5.6%, 3.6%, and 0.4%, respectively in
233 order of decreasing abundance. The high proportion of clay minerals in the shale of the Gulong
234 Sag distinguishes it from other types of shales. Intergranular pores develop between mineral
235 grains and crystals, including quartz, feldspar, carbonates, and clay (Loucks et al., 2010). This
236 pore type is profitable for the formation of high reservoir quality, followed by intraparticle pores.
237 Additionally, intragranular pores can usually be detected in particles, including in feldspar and
238 pyrite (Loucks et al., 2010; Milliken et al., 2013). Organic matter pores can be detected in
239 organic matters with small diameters (Loucks et al., 2010; Kuila et al., 2014; King et al., 2015).

240 The dominant lithologies are shale, mudstone, siltstone, shell limestone, and dolostone
241 (Fig. 6). Gray-black shales are characterized by multi-scale laminae (the laminae density).
242 Gray-white siltstones observed with laminae in cores accounted for a bit proportion. Only 1 m

243 thickness of siltstones are observed in Well Y among all these five key studied wells. Well Y.
244 The siltstones are attributed to terrigenous clastic input during an episode of falling lake level
245 (Liu et al., 2019; Lin et al., 2021). Dolostone and bioclastic limestone are present in gray-white
246 colors in the cores, accounting for 16%. Moreover, palaeobiota and palaeoflora (shell, algae)
247 are preserved in the limestone, which can be identified by hydrochloric acid.

248 The oil shale reservoir in the Qingshankou Formation of the Gulong Sag, Songliao Basin,
249 has a high reservoir quality characterized by an effective porosity of 0.5–12.1%, with an
250 average value of 7.0% (Fig. 7). The total porosity ranges from 1.2% to 14.4%, with an average
251 value of 9.5% (Fig. 7). The “sweet spot”, distributed in the first Member and the lower part of
252 the second Member in the Qingshankou Formation, is characterized by a total porosity of 6.2%
253 –11.6%, with an effective porosity of 2.3%–7.1% (Cui et al., 2020). The main reservoir space
254 consists of a great abundance of nanopores and a small number of micropores. Microfractures
255 improve the reservoir seepage capacity (Li et al., 2017).

256

257 **4.2. Multi-scale lamina structure**

258 **4.2.1. Three types of lamina structure**

259 The multi-scale lamina can be divided into three types, including laminated rocks (the
260 thickness of the layer is less than 0.01 m), layered rocks (the bundles of genetically related
261 laminae thickness ranging between 0.01 m–0.1 m), and massive rocks (no varve or layer
262 spacing > 0.1 m) according to the core observation (Fig. 8). However, there are a few
263 differences in various lithologies. All laminated rocks, layered rocks, and barely massive rocks
264 can be observed in shales. Three types of laminae can be observed in siltstone, but only massive

265 rocks appear in mudstone, limestone, and dolostone (Fig. 6). Furthermore, laminated rocks can
266 be classified into bright lamina (carbonate lamina and felsic lamina) and dark lamina (organic
267 lamina and clay mineral lamina) according to the mineral assemblage through the microscopic
268 inspection in shale reservoirs (Fig. 6). The different bright and dark laminae consist of various
269 lamina structures based on their superposition sequence, which indicates the sedimentary
270 processing and environment (Dräger et al., 2016). Lamina records have been shown to provide
271 reliable records of spring discharges and variability therein (Sander et al., 2002). Lamina
272 structure records are preserved in fine-grained sedimentary rocks providing possibilities for
273 high-resolution climatic and environmental reconstructions (Jokinen et al., 2015; Haltia et al.,
274 2021).

275

276 **4.2.2. Well log expressions of various lamina**

277 In addition, there are many studies about the interpretation of the lamina record and
278 information preserved in its layers (Haltia et al., 2021). However, the continuous expressions
279 of lamina preserved in the reservoir (especially in shale oil and gas) remain scarce. A new
280 method is proposed to continuously evaluate the lamina in a single well as the development of
281 the new techniques. The slab and the button electrode curve derived from image logs with the
282 highest resolution in well logging technologies are used to identify and classify the lamina types
283 (Fig. 9, Table. 1). The dynamic slabs of image logs show the layer alternately exchange in color
284 gradation (bright, orange, dark, and intermediate color) (Fig. 9). The button conductivity curve
285 characterizes the layer in the form of both color gradation and amplitude variation of the curve
286 (Fig. 9).

287 In laminated rocks, the thickness of a single layer is on a millimeter scale, indicating the
288 laminae changes are less than 1 centimeter. A total of 59 layers can be observed in different
289 colors within 0.5 meters (Fig. 9A). More than 84 amplitude variations (peaks and troughs) can
290 be identified in 0.5 meters (Fig. 9A). It can be observed that the button conductivity curve
291 shows serrated characterization (Fig. 9A).

292 The layered rocks show that the thickness of the individual layer is centimeter-scale,
293 ranging from 1 centimeter to 10 centimeters, suggesting that the layers' changes are centimeter
294 lamination. A total of 35 layers can be recognized on the slab, and almost 71 layers are observed
295 on the button conductivity curve in 0.5 meters (Fig. 9B).

296 No layers in the massive rocks or the individual layer of massive rocks is greater than 10
297 centimeters. There are no layers that can be observed in 0.1-meter scale depth intervals in slab
298 images, but thinner layers can be detected by the button conductivity curve (Fig. 9C). In
299 addition, the button electrode curve exhibits a box-shaped feature (Fig. 9C). The mudstone and
300 limestone/dolostone of massive rocks are characterized by the image logs or slabs with single
301 dark and bright spots, respectively.

302 Shales were dominated by laminated rocks and layered rocks observed from core photos
303 and characterized by FMI images especially slabs (Fig. 10A–10D). According to core
304 observation, the interface between different laminae was flat and intermittent in shales (Fig.
305 10A–10D). The shales accounted for the most proportion of rocks in the Qingshankou
306 Formation. Only massive rocks can be observed in mudstones, without obvious layers or
307 laminae and the FMI images display a dark spot model (Fig. 10E). Three types of lamina
308 structure can be detected in sandstones (Fig. 10F–10H). The boundary between various bedding

309 is clear, and the interface was horizontal or wave and continuous (Fig. 10F–10H). From the
310 core observation, laminated and layered rocks rarely appear in limestones and dolostones and
311 the FMI images show a bright spot model (Fig. 10I). Via insight through the FMI image, the
312 shale and mudstones are characterized by dark color in the static images (Fig. 10A–10E),
313 whereas the static images display organic-yellow color in siltstones (Fig. 10F–10H). In
314 addition, the FMI images show bright color pattern in limestones and dolostones (Fig. 10I).
315 From the thin section observation, four types of laminae were identified, including clay lamina,
316 felsic lamina, organic mineral lamina, and carbonate lamina (Fig. 10J).

317

318 **4.2.3. T₁-T₂ maps obtained from NMR logs**

319 Previous studies have established the classification scheme for grouping different
320 hydrogen-bearing components in shales according to the NMR experiment (Kausik et al., 2016;
321 Li et al., 2018; Mukhametdinova et al., 2021). These groups include kerogen, absorbed oil, free
322 oil, structural water, absorbed water, free water, bulk oil and bulk water. However, NMR
323 logging only responds to the formation of pore fluid without the effect of kerogen content.
324 According to the T₂ and the ratio of T₁ to T₂ response of different fluid types, oil-bearing
325 properties and mobility will be qualitatively and quantitatively characterized and evaluated. In
326 this study, the oil-bearing property and reservoir quality were qualitatively evaluated by the
327 location of energy clusters (hydrogen clusters). The energy cluster located in the upper-right
328 corner of the T₁-T₂ map represents high reservoir quality and high oil saturation. On the contrary,
329 the energy cluster located in the lower-left corner of the T₁-T₂ map indicates poor reservoir
330 quality and low movable oil and water content (Fig. 11). Based on the lamina structure

331 classification in the Cretaceous Qingshankou Formation in the Gulong Sag, Songliao Basin,
332 three types of T_1 - T_2 maps were identified in well Z.

333 Type I T_1 - T_2 map of laminated rocks is characterized by two main energy clusters, the
334 lower-left corner and the upper-right corner, representing different fluid types in various pore
335 systems (Fig. 11A). The left corner energy cluster shows clay-bound water and bitumen in the
336 intragranular pores and organic matter pores. The energy cluster in the right corner represents
337 the movable water ($T_1 = T_2$, yellow-green parts) and movable oil ($T_1 > T_2$, red parts), indicating
338 well oil-bearing property. Both the T_1 and T_2 distributions exhibit bimodal behaviors, implying
339 the strong heterogeneous of laminated rocks. The short T_2 components represent the
340 discontinuous pores of small sizes. The T_2 components larger than 30 ms correspond to the
341 large pores (dissolution pores) and well connectivity pores and throats, resulting in the good
342 reservoir quality (Lai et al., 2019).

343 Type II T_1 - T_2 map corresponding to layered rocks shows three clusters, the lower-left
344 corner, the upper right corner, and the part along the waterline ($T_1 = T_2$) (Fig. 11B). The left
345 corner part is located lower than in laminated rocks and near the waterline due to more
346 immovable water in small pores. The part alongside the waterline is characterized by movable
347 water in connectivity pore space. The energy intensity of the upper right corner is lower than in
348 laminated rocks, which displays in green color rather than red.

349 The energy cluster of type III representing massive rocks, the T_1 - T_2 map, is concentrated
350 in the lower-left corner (short T_1 and T_2 components), representing bitumen, clay bound water,
351 and oil in organic porosity (Fig. 11C). The T_2 spectrum shows unimodal behavior. The T_2
352 relaxation time is restricted to within a narrow range (< 30 ms), indicating more pores of small

353 sizes lacking large pores. Obviously, this type of rock corresponds with poor reservoir quality.

354

355 **5. Discussion**

356 **5.1. Lamina distribution prediction via well logs**

357 The dominant laminae structure is layered rocks, followed by laminated rocks, with only
358 a small number of instances of massive rocks identified in the Cretaceous Qingshankou
359 Formation in Well X (Fig. 12). In total, 1,178 layers are identified in the 482.5 m thickness
360 Qingshankou Formation of Well X. 482 layers of laminated rocks account for 45% thickness,
361 and the thickness of a single layer ranges from 0.04 m to 2.92 m with an average value of 0.45
362 m. The layered rocks, with the maximum proportion of 50.4% thickness in these three types,
363 comprise 563 layers, and the average thickness of each layer is 0.43 m ranging from 0.02 m to
364 5.23 m. Only 4.6% of the massive rocks are recognized, containing 133 layers.

365 In contrast, laminated rocks account for the largest proportion in Well Y. In total, 453 layers
366 are identified in the 136.8 m thickness in the Qingshankou Formation (Q1-Q9). In total, 198
367 layers of laminated rocks with 80.08 m thickness are recognized, and single layers range in
368 thickness from 0.07 m to 20.2 m, with an average of 0.4 m. There are 183 layers of layered
369 rocks with 47.57 m thickness, and the average thickness of every single layer is 0.26 m (the
370 minimum of 0.04 m and the maximum of 0.95 m). Only 72 layers of massive rocks can be
371 classified in Well Y, and their total cumulative thickness is 9.15 m.

372 From the distribution prediction via well logs above, it can be concluded that laminated
373 rocks and layered rocks are the main laminae structure in the Cretaceous Qingshankou
374 Formation in Gulong Sag Songliao Basin. The laminae development makes it unique from other

375 types of shale worldwide, for example the Barnett Shale in the Fort Worth Basin in the United
376 States, the Permian Lucaogou Formation in Jimusar Sag in Junggar Basin in China , and the
377 Triassic Yanchang Formation in the Ordos Basin in China (Loucks et al., 2009; Xi et al., 2015,
378 2020; Zou et al., 2019).

379 There is a specific correspondence between the conventional well logs and the lamina
380 structure (Wang et al., 2021). The massive rocks contain high carbonate content, corresponding
381 to high resistivity and low gamma values (Fig. 12). Conversely, the laminated rocks are
382 characterized by high gamma value attributed to the high content of clay minerals. The layered
383 rocks contain more felsic resulting in medium resistivity and gamma value. The main
384 controlling factors of various lamina types are complex, including climate change, lake level
385 fluctuation, and the injection of terrigenous detritus (Fagel et al., 2021). In addition, it can be
386 observed from Fig. 12 that the resolution of the conventional well logs is low, and the curves
387 change gently. Therefore, it is challenging to identify the lamina structure through the
388 conventional well logs. However, the high-resolution image logs (5 mm) are profitable for
389 evaluating lamina structure, especially the slabs and button conductivity curve derived from the
390 image logs.

391

392 **5.2. Prediction of lamina structure as a control on reservoir quality and oil content**

393 T_1 - T_2 maps obtained from the NMR logs can be used to describe the fluid types, oil-
394 bearing, and porous systems (Guo et al., 2020; Ge et al., 2022; Pang et al., 2022). In our study,
395 the T_1 - T_2 maps are divided into three types corresponding to three types of lamina structure.

396 Figure 13 shows the lamina structure distribution and corresponding T_1 and T_2 spectra of

397 the Cretaceous Qingshankou Formation in Well Y. The interpretation interval A is typical
398 layered rocks. The T_1 - T_2 map is characterized by two energy clusters, the left corner in red color,
399 a little away from the center, representing less immovable fluid (Fig. 13A). The upper right
400 corner in green color implies less movable fluid than the right corner in red color (Fig. 13A).
401 Consequently, the T_1 - T_2 map of interval A shows higher reservoir quality and better oil-bearing
402 properties. The massive rocks mainly correspond with intervals with short T_2 components, and
403 the T_1 - T_2 map shows only one energy cluster in the lower left (Fig. 13B). Interval C, the same
404 as interval A, is representative layered rocks (Fig. 13C). The laminated rocks are related to the
405 intervals with long T_2 distribution and high amplitudes but lower than layered rocks. In addition,
406 two energy clusters can be observed in the T_1 - T_2 map, and the upper right corner cluster is in
407 green, indicating the good reservoir quality and oil-bearing potential (Fig. 13D).

408 Interpretation interval A is a representative layered rock, and the T_2 spectra exhibit a long
409 T_2 relaxation time with high amplitude (Fig. 14A). Two energy clusters can be observed in the
410 T_1 - T_2 map indicating the good reservoir quality and oil mobility (Fig. 14A). The interval B is a
411 typical laminated rock (Fig. 14B). The T_2 spectra show a long T_2 relaxation time but lower
412 amplitude in the long T_2 components (Fig. 14B). There are two energy clusters in the T_1 - T_2 map,
413 but the energy is weak in the upper right corner implying less oil mobility (Fig. 14B). Therefore,
414 from investigating the relationships between lamina structure and NMR logs (T_2 distribution
415 and T_1 - T_2 maps), the layered rocks have the best reservoir quality and most favorable oil-
416 bearing properties in the shales, followed by laminated rocks.

417 Additionally, the oil test can approve these conclusions that the more layered rocks
418 develop, the better reservoir quality and oil yield productivity are (Fig. 14C, 14D). The oil test

419 results show that Well Z is more productive than Well Y (Fig. 14C, 14D). The laminated rocks
420 account for 42.1%, and the layered rocks is 49.9% in the Qingshankou Formation (strata Q3 to
421 Q4) in well Z (Fig. 14C). However, the laminated rock's proportions are up to 67.1%, and the
422 layered rocks account for 27.9% in well Y (strata Q3 to Q4) (Fig. 14D).

423 The lamina structure and oil-bearing properties are interpreted in Well Z (Fig. 15).
424 Interpretation intervals A and D are typical laminated rocks, which show different T_1 - T_2 maps.
425 Interval A exhibits better reservoir quality and oil potential than interval B, attributed to the less
426 clay mineral content (Fig. 15). The intervals B and C are representative layered rocks, whereas
427 the reservoir quality of interval C is better than interval B since there are fewer clay minerals
428 (Fig. 15). Therefore, from investigating the relationships between lamina structure, mineral
429 composition, and T_1 - T_2 maps, the reservoir quality and oil-bearing properties increase with
430 decreasing clay mineral content in shales in different lamina structures.

431 In addition, oil is mainly distributed in the interface between mudstone and sandstone or
432 carbonate, but less in carbonate or sandy layers (Shao et al., 2021). Light components of high
433 mature oil are relatively accumulated in carbonate or felsic laminae, while heavy components
434 are relatively enriched in clay or organic matter laminae (Shao et al., 2021; Zhang et al., 2021).

435 However, the controlling factors of reservoir quality are complicated. The layered rocks
436 combined with high content of organic matter, favorable lithofacies, and fractures (including
437 parallel fractures) may lead to a high-quality reservoir and oil mobility.

438

439 **6. Conclusions**

440 This study elucidates the relationship between lamina structure, reservoir quality, and oil

441 potential in shale, taking the Cretaceous Qingshankou Formation in Gulong Sag, Songliao
442 Basin, as an example.

443 The main mineralogical compositions of the shales in the Qingshankou Formation are
444 quartz, feldspar, clay minerals, and a small number of carbonates. According to the core
445 observation in oil shale, the lamina structure is classified into three types: laminated rocks,
446 layered rocks, and massive rocks. Both laminated rocks and layered rocks can be observed in
447 shales, but on rarely massive rocks can be observed. Three types of laminae can be observed in
448 siltstone, but only massive rocks appear in mudstone, limestone, and dolostone. The image logs,
449 slabs, and button conductivity curves are efficient ways to predict a single well's lamina
450 distribution. The Qingshankou Formation is dominated by laminated rocks and layered rocks,
451 which account for more than 90 percent. According to the energy clusters, the T_1 - T_2 maps are
452 classified into three types: type I, II, and III, which correspond to laminated rocks, layered rocks
453 and massive rocks, respectively. Among all the lamina structures, layered rocks show a good
454 reservoir quality and high oil accumulation, followed by laminated rocks. In contrast, massive
455 rocks present a poor reservoir quality without oil production. The greater the clay mineral
456 content, the poorer the quality and oil potential of the shale reservoirs.

457

458 **Acknowledgments**

459 This work was supported by the PetroChina Research Institute of Petroleum Exploration
460 and Development and PetroChina Daqing Oilfield Company. We would like to give our sincere
461 gratitude to them for providing samples and data access. The authors would also like to thank
462 the National Natural Science Foundation of China (Grant No. 42002133, 42072150) for the

463 financial support and permission to publish this paper. We sincerely appreciate the American
464 Association of Petroleum Geologists Foundation and the Southeast Asia Petroleum Exploration
465 Society Grant. We appreciate the editorial staff and all four reviewers for their diligent work
466 with enthusiasm and patience.

467

468 **References**

- 469 Bechtel, A., J. Jia, S. A. I. Strobl, R. F. Sachsenhofer, Z. Liu, R. Gratzner, and W. Püttmann, 2012,
470 Palaeoenvironmental conditions during deposition of the Upper Cretaceous oil shale sequences
471 in the Songliao Basin (NE China): Implications from geochemical analysis. *Organic*
472 *Geochemistry*, 46, 76–95.
- 473 Bize E., Karoon A T., Laronga R., Bize-Forest N. 2015. Virtual Core: State-of-the-Art Wireline
474 Technologies To Provide a Viable Substitute for Whole Conventional Coring. Offshore
475 Technology Conference.
- 476 Brauer A and Casanova J. 2001. Chronology and depositional processes of the laminated sediment
477 record from Lac d'Annecy, French Alps. *Journal of Paleolimnology* 25(2): 163–177.
- 478 Chen F W., Lu S F., Huang Z K., Wang W W., Xie Z., Xiao H. 2013. Sedimentary characteristics
479 and favorable exploration zone of K1qn1 in Gulong Depression of Songliao Basin. *Journal of*
480 *Central South University (Science and Technology)*, 44, 5, 1955–1963.
- 481 Chen, S.Y., Zhang, S., Liu, H.M., Yan, J.H. 2017. Discussion on mixing of fine-grained
482 sediments in lacustrine deep water. *Journal of Paleogeography*, 19(2), 271–283.
- 483 Cui Baowen., Chen Chunrui., Lin Xudong., Zhao Ying., Cheng Xinyang., Zhang Yupeng., Lu
484 Guoqiang. 2020. Characteristics and distribution of sweet spots in Gulong shale oil reservoirs

485 of Songliao Basin. *Petroleum Geology & Oilfield Development in Daqing*, 39, 3, 45–55.

486 Dräger Nadine., Theuerkauf Martin., Szeroczyńska Krystyna., Wulf Sabine., Tjallingii Rik., Plessen
487 Birgit., Kienel Ulrike., Brauer Achim. 2016. Varve microfacies and varve preservation record
488 of climate change and human impact for the last 6000 years at Lake Tiefer See (NE Germany).
489 Research Paper, *The Holocene*, 1–15.

490 Fagel N., Pedreros P., Alvarez D., Tylmann W., Namur O., Da Silva A C., Jana P., Araneda A., Billy
491 I., Schmidt S., Urrutia R. 2021. Last millennium climate variability of the varved Lake
492 Jeinimeni geochemical record from NE Chilean Patagonia. *Quaternary Science Reviews*, 269,
493 107134.

494 Feng Z H., Liu B., Shao H M., Wang C., Hong S X., Wang J P., Pan H F., Wang Y C., Zhang A D.,
495 Tian S S., Chi Y A. 2020. The diagenesis evolution and accumulating performance of the mud
496 shale in Qingshankou Formation in Gulong area, Songliao Basin. *Petroleum Geology &
497 Oilfield Development in Daqing*, 39, 3, 72–85.

498 GE Rongfeng., ZHANG Qinglong., WANG Liangshu., XIE Guo'ai., XU Shiyin., CHEN Juan.,
499 WANG Xiyong. 2010. Tectonic Evolution of Songliao Basin and the Prominent Tectonic
500 Regime Transition in Eastern China. *Geological Review*, 56, 2, 180–193.

501 Ge Xinmin, Zhang Renxia, Liu Jianyu, Fan Yiren, Zhao Jier, Li Chaoliu, Hu Falong. 2022. NMR
502 transverse relaxation of the clay-rich shale in inhomogeneous magnetic field: A numerical
503 study. *Computers & Geosciences*, 166, 105174.

504 Guo J F., Xie R H., Xiao L Z. 2020. Pore-fluid characterizations and microscopic mechanisms of
505 sedimentary rocks with three-dimensional NMR: Tight sandstone as an example. *Journal of
506 Natural Gas Science and Engineering*, 80,103392.

507 Haltia E., Leppanen A P., Kallio A., Saarinen T. 2021. Sediment profile dating and reconstructing
508 nuclear events from annually laminated lake sediments in northern Finland. *Journal of*
509 *Environmental Radioactivity*, 233, 106611.

510 Hill, R.J., Zhang, E., Katz, B.J., et al. Modeling of gas generation from the Barnett shale, fort Worth
511 basin, Texas. *AAPG Bulletin*, 2007, 91, 4, 501–521.

512 Hou Lianhua., Zou Caineng., Yu Zhichao., Luo Xia., Wu Songtao., Zhao Zhongying., Lin Senhu.,
513 Yang Zhi., Zhang Lijun., Wen Dingwei., Cui Jingwei. 2021. Quantitative assessment of the
514 sweet spot in marine shale oil and gas based on geology, engineering, and economics: A case
515 study from the Eagle Ford Shale, USA. *Energy Strategy Reviews*, 38, 100713.

516 Jarvie, D.M., Hill, R.J., Ruble, T.E. Unconventional shale-gas systems: the Mississippian Barnett
517 Shale of north-central Texas as one model for thermogenic shale-gas assessment. *AAPG*
518 *Bulletin* 2007, 91, 475–499.

519 Jokinen A., Sami, Virtasalo J., Joonas, Kotilainen T., Aarno, Saarinen, Timo, 2015. Varve
520 microfabric record of seasonal sedimentation and bottom flow-modulated mud deposition in
521 the coastal northern Baltic Sea. *Marine Geology*, 366, 79–96.

522 Kausik, R., Fella, K., Rylander, E., Singer, P.M., Lewis, R.E., Sinclair, S.M., 2016. NMR
523 relaxometry in shale and implications for logging. *Petrophysics* 57, 339–350.

524 King Jr HE, Eberle AP, Walters CC, Kliewer CE, Ertas D, Huynh C. 2015. Pore architecture and
525 connectivity in gas shale. *Energy & Fuels*, 29, 1375–1390.

526 Ko, L.T., Loucks, R.G., Ruppel, S.C., et al. Origin and characterization of Eagle Ford pore networks
527 in the south Texas Upper Cretaceous shelf. *AAPG Bulletin* 2017,101 (3), 387–418.

528 Kuila U, McCarty DK, Derkowski A, Fischer TB, Top'or T, Prasad M. 2014. Nano-scale texture

529 and porosity of organic matter and clay minerals in organic-rich mudrocks. *Fuel*, 135, 359–73.

530 Kumar A., Laronga R., Kherroubi J., Bringer F., Kear G., Herrera J. 2014. Visualizing Borehole
531 Images in a Slabbed-Core Format. EAGE, Borehole Geology Workshop, 12–15.

532 Lai Jin., Liu Bingchang., Li Hongbin., Pang Xiaojiao., Liu Shichen., Bao Meng., Wang Guiwen.
533 2022a. Bedding parallel fractures in fine-grained sedimentary rocks: recognition, formation
534 mechanisms, and prediction using well log. *Petroleum Science*,
535 <https://doi.org/10.1016/j.petsci.2021.10.017>

536 Lai J., Pang X., Xu F., Wang G., Fan X., Xie W., Chen J., Qin Z., Zhou Z. 2019. Origin and formation
537 mechanisms of low oil saturation reservoirs in Nanpu Sag, Bohai Bay Basin, China. *Marine
538 and Petroleum Geology* 110, 317–334.

539 Lai J., Wang G., Fan Q., et al. 2022b. Geophysical Well-Log Evaluation in the Era of
540 Unconventional Hydrocarbon Resources: A Review on Current Status and Prospects. *Surveys
541 in Geophysics*, 43:913–957

542 Lai J., Wang G., Wang S., Cao J., Li M., Pang X., Han C., Fan X., Yang L., He Z., Qin, Z. 2018. A
543 review on the applications of image logs in structural analysis and sedimentary characterization.
544 *Marine and Petroleum Geology*, 95, 139–166.

545 Li Canxing., Liu Dongdong., Xiao Lei., Jiang Zhenxue., Li Zhuo., Guo Jing. 2021a. Research into
546 pore evolution in Cretaceous continental shales in the Songliao Basin. *Petroleum Science
547 Bulletin*, 2, 181–195.

548 Li F., Zhao W Y., Guo A J., Chang T Y. 2021b. Quantitative characterization of rock pore structure
549 and its computer application: a case study of Qingshankou Formation in Songliao Basin. *Coal
550 Engineering*, 53, 7, 119–122.

551 Li J., Wang M., Lu S., Chen G., Tian W., Jiang C., Li Z. 2020. A new method for predicting
552 sweet spots of shale oil using conventional well logs. *Marine and Petroleum Geology*, 113,
553 104097.

554 Li Jinbu., Huang Wenbiao., Lu Shuangfang., Wang Min., Chen Guohui., Tian Weichao., Guo
555 Zhiqiang. 2018. Nuclear Magnetic Resonance T_1 – T_2 Map Division Method for Hydrogen-
556 Bearing Components in Continental Shale. *Energy&Fuel*, 32, 9043–9054.

557 Li Maowen., Ma Xiaoxiao., Jiang Qigui., Li Zhiming., Pang Xiongqi., Zhang Caitong. 2019.
558 Enlightenment from formation conditions and enrichment characteristics of marine shale oil in
559 North America. *Petroleum Geology and Recovery Efficiency*, 26, 1, 13–28.

560 Li S C., Zhang J Y., Gong F H., Zhu H., Bai Y F. 2017. The characteristics of mudstones of Upper
561 Cretaceous Qingshankou Formation and favorable area optimization of shale oil in the north
562 of Songliao Basin. *Geological Bulletin of China*, 36, 4, 654–663.

563 Lin Y F., Bai Y F., Zhao Y., Cheng X Y., Lv J C., Liu Z. 2021. Cyclic stratigraphy of fine-grained
564 sedimentary rocks and sedimentary filling response characteristics of Member Qing-1 in
565 Gulong Sag, Songliao Basin. *Petroleum Geology & Oilfield Development in Daqing*, 40, 5,
566 29–39.

567 Liu B., Wang H L., Fu X F., Bai Y F., Bai L H., Jia M C., He B. 2019. Lithofacies and depositional
568 setting of a highly prospective lacustrine shale oil succession from the Upper Cretaceous
569 Qingshankou Formation in the Gulong sag, northern Songliao Basin, northeast China. *AAPG*
570 *Bulletin*, 103, 2, 405–432.

571 Loucks, R. G., Reed, R. M., Ruppel, S. C., and Hammes, U. 2010, Preliminary classification of
572 matrix pores in mudrocks: *Gulf Coast Association of Geological Societies Transactions*, 60,

573 435–441.

574 Loucks, R. G., Reed, R. M., Ruppel, S. C., Jarvie, D. M., 2009. Morphology, genesis, and
575 distribution of nanometer-scale pores in siliceous mudstones of the Mississippian Barnett shale.
576 *Journal of Sedimentary Reservoir*, 79, 848–861.

577 Marc Fleury., MariaRomero-Sarmiento. 2016. Characterization of shales using T1–T2 NMR maps.
578 *Journal of Petroleum Science and Engineering*, 137, 55–62.

579 Milliken KL, Rudnicki M, Awwiller DN, Zhang T. 2013. Organic matter–hosted pore system,
580 Marcellus formation (Devonian). Pennsylvania, *AAPG Bulletin*, 97, 177–200.

581 Mukhametdinova Aliya., Iwona Habina-Skrzyniarz., Andrey Kazak., Artur Krzyzak. 2021. NMR
582 relaxometry interpretation of source rock liquid saturation — A holistic approach. *Marine and*
583 *Petroleum Geology*, 132, 105165.

584 Newport, L. P., A. C. Aplin, J. G. Gluyas, H. C. Greenwell, and D. R. Gröcke, 2016. Geochemical
585 and lithological controls on a potential shale reservoir: Carboniferous Holywell Shale, Wales:
586 *Marine and Petroleum Geology*, 71, 198–210.

587 Pang Xiaojiao., Wang Guiwen., Kuang Lichun., Li Hongbin., Zhao Yidi., Li Dong., Zhao Xin., Wu
588 Songtao., Feng Zhou., Lai Jin. 2022. *Marine and Petroleum Geology*, 137, 105492.

589 Pang Y M., Zhang Y Q., Cai M., Zhang H L., Guo Z Q. 2021. Technical and economic limit of
590 horizontal well development for Gulong shale oil in Songliao Basin. *Petroleum Geology &*
591 *Oilfield Development in Daqing*, 40, 5, 134–143.

592 Saidian, M., & Prasad, M. 2015. Effect of mineralogy on nuclear magnetic resonance surface
593 relaxivity: A case study of Middle Bakken and Three Forks formations. *Fuel*, 161, 197-206.

594 Sander, M., Bengtsson, L., Holmquist, B., Wohlfarth, B., Cato, I., 2002. The relationship between

595 annual varve thickness and maximum annual discharge. *Journal of Hydrology*, 263, 23–35.

596 Shao Hongmei., Gao Bo., Hong Shuxin., Li Lingling., Wang Jiping., Wang Yongchao., Bai Xuejing.,
597 Tan Wenli. 2021. Progress and application of the experimental technologies for the shale oil
598 reservoirs: A case study on Gulong area in Songliao Basin. *Petroleum Geology & Oilfield*
599 *Development in Daqing*, 39, 3, 97–106.

600 Soeder. D.J. 2017. The successful development of gas and oil resources from shales in North
601 America, *Journal of Petroleum Science and Engineering*, 163, 399-420.

602 Sun Longde., Liu He, He Wenyuan., Li Guoxin., Zhang Shuichang., Zhu Rukai., Jin Xu., Meng
603 Siwei., Jiang Hang. 2021. An analysis of major scientific problems and research paths of
604 Gulong shale oil in Daqing Oilfield, NE China. *Petroleum Exploration and Development*. 48,
605 3, 527–540.

606 Tang Xianglu., Jiang Shu., Jiang Zhenxue., Li Zhuo., He Zhiliang., Long Shengxiang., Zhu Deyu.
607 2019. Heterogeneity of Paleozoic Wufeng-Longmaxi formation shale and its effects on the
608 shale gas accumulation in the Upper Yangtze Region, China. *Fuel*, 239, 387–402.

609 Wang Song., Wang Guiwen., Huang Liliang., Song Lianteng., Zhang Yilin., Li Dong., Huang Yuyue.
610 2021. Logging evaluation of lamina structure and reservoir quality in shale oil reservoir of
611 Fengcheng Formation in Mahu Sag, China. *Marine and Petroleum Geology*, 133, 105299.

612 Weidlich O., Bernecker M. 2004. Quantification of depositional changes and paleo-seismic
613 activities from laminated sediments using outcrop data. *Sedimentary Geology*, 166, 11–20.

614 Xavier Boe's., Nathalie Fagel. 2005. Impregnation method for detecting annual laminations in
615 sediment cores: An overview. *Sedimentary Geology*, 179, 185–194.

616 Xi, K.L., Cao, Y.C., Zhu, R.K., Shao, Y., Xue, X.J., Wang, X.J., Gao, Y., Zhang, J., 2015. Rock types

617 and characteristics of tight oil reservoir in permian Lucaogou Formation, Jimsar sag. *Acta Pet.*
618 *Sin.* 36, 1495–1507 (in Chinese with English abstract).

619 XI Kelai., LI Ke., CAO Yingchang., LIN Miruo., NIU Xiaobing., ZHU Rukai., WEI Xinzhuo., YOU
620 Yuan., LIANG Xiaowei., FENG Shengbin. 2020. Laminae combination and shale oil
621 enrichment patterns of Chang 73 sub-member organic-rich shales in the Triassic Yanchang
622 Formation, Ordos Basin, NW China. *Petroleum Exploration and Development*, 47, 6, 1244–
623 1255.

624 Xu Chenyu, Xie Ranhong, Guo Jiangfeng, Jin Guowen, Fan Wenshuai, Xiao Lizhi. 2023,
625 Comprehensive characterization of petrophysical properties in shale by solvent extraction
626 experiments and 2D NMR. *Fuel*, 335, 127070.

627 Xu, J., A. Bechtel, R. F. Sachsenhofer, Z. Liu, R. Gratzel, Q. Meng, and Y. Song, 2015, High
628 resolution geochemical analysis of organic matter accumulation in the Qingshankou Formation,
629 Upper Cretaceous, Songliao Basin (NE China): *International Journal of Coal Geology*, 141–
630 142, 23–32.

631 Yang Zhi., Zou Caineng., Wu Songtao., Lin Senhu., Pan Songqi., Niu Xiaobing., Men Guangtian.,
632 Tang Zhenxing., Li Guohui., Zhao Jiahong., Jia Xiyu. 2019. Formation, distribution and
633 resource potential of the "sweet areas (sections)" of continental shale oil in China. *Marine and*
634 *Petroleum Geology*, 102, 48–60.

635 Zhang Anda., Wang Jiping., Wang Yongchao., Hong Shuxin., Tan Wenli. 2021. Reservoir space
636 types and oil occurrence of Gulong shale in Songliao Basin. *Petroleum Geology & Oilfield*
637 *Development in Daqing*, 40, 5, 68–77.

638 Zhang Pengfei., Lu Shuangfang., Li Junqian., Chang Xiangchun. 2020. 1D and 2D Nuclear

639 magnetic resonance (NMR) relaxation behaviors of protons in clay, kerogen and oil-bearing
640 shale rocks. *Marine and Petroleum Geology*, 114, 104210.

641 Zhou, Y., and R. Littke, 1999, Numerical simulation of the thermal maturation, oil generation and
642 migration in the Songliao Basin, Northeastern China. *Marine and Petroleum Geology*, 16, 8,
643 771–792.

644 Zou Caineng., Ding Yunhong., Lu Yongjun., Liu Xiangui., Chen Jianjun., Wang Xin., Yang
645 Zhengming., Cai Bo., Yang Zhi., He Chunming., Wang Zhen., Luo Yutian. 2017. Concept,
646 technology and practice of “man-made reservoirs” development. *Petroleum Exploration and
647 Development*, 44, 1, 144–154.

648 Zou Caineng., Yang Zhi., Cui Jingwei., Zhu Rukai., Hou Lianhua., Tao Shizhen., Yuan Xuanjun.,
649 Wu Songtao., Lin Senhu., Wang Lan., Bai Bin., Yao Tingli. 2013. Formation mechanism,
650 geological characteristics and development strategy of nonmarine shale oil in China. *Petroleum
651 Exploration and Development*, 40, 1, 14–26.

652 Zou, C.N., Zhu, R.K., Chen, Z.Q., Ogg, J.G., Wu, S.T., Dong, D.Z., Qiu, Z., Wang, Y.M., Wang, L.,
653 Lin, S.H., Cui, J.W., Su, L., Yang, Z. 2019. Organic-matter-rich shales of China. *Earth Science
654 Review*, 189, 51–78.

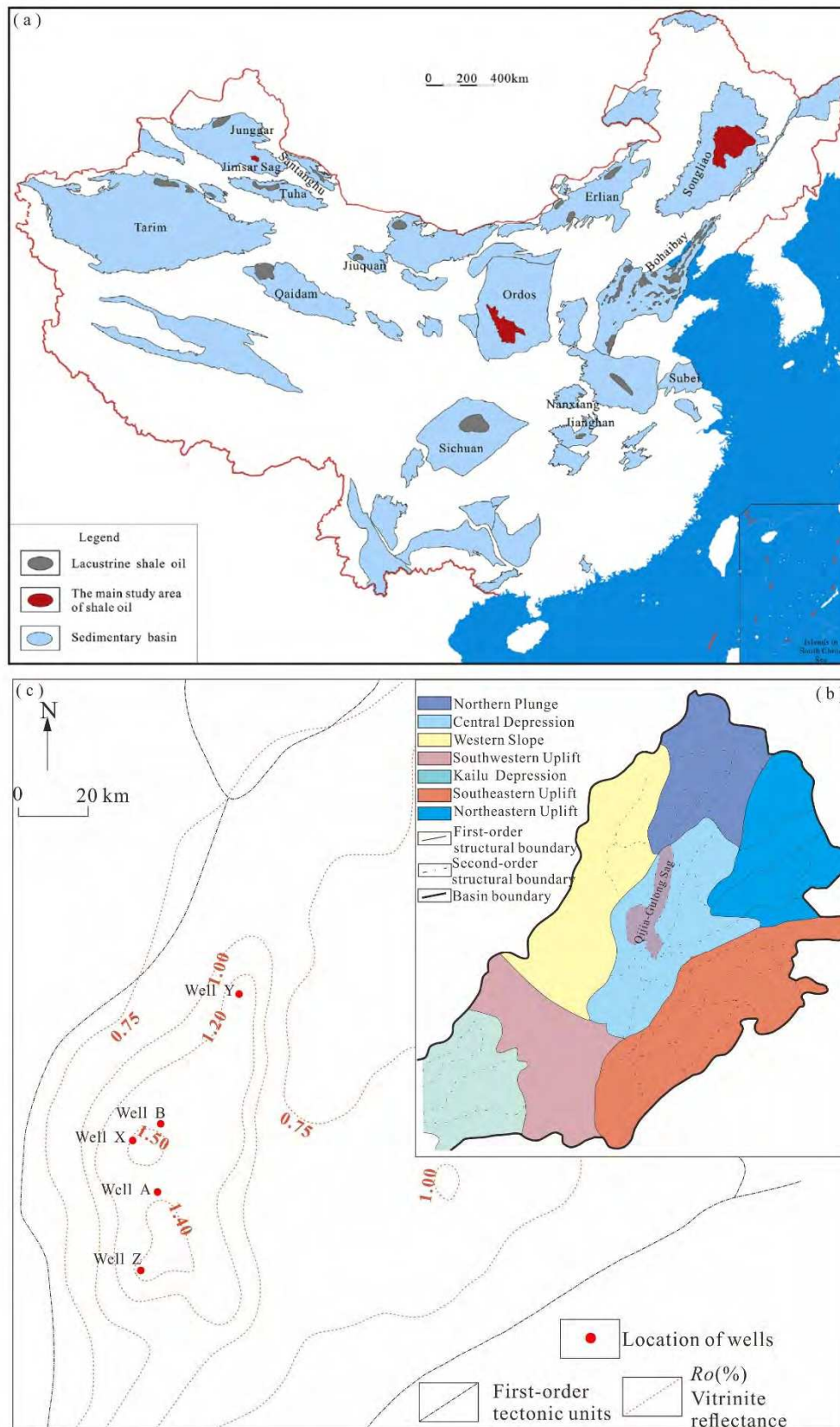


Figure 1. Location and geological map of Gulong Sag in Songliao Basin: (a) the Songliao Basin in China; (b) the location of Gulong Sag in Songliao Basin; (c) the location of the examined wells (Modified from Yang et al., 2019; Li et al., 2021).

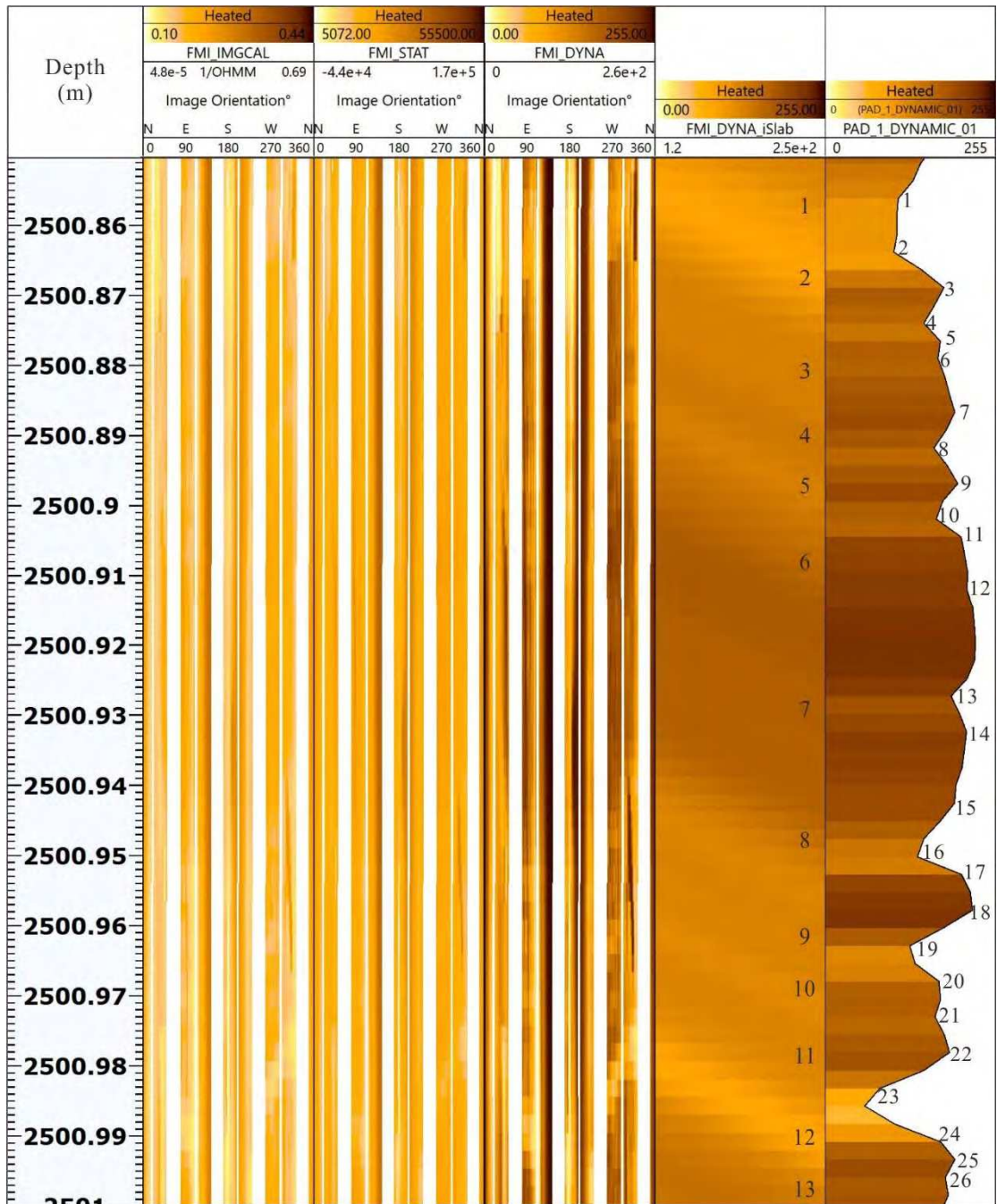


Figure 2. Slab image and button electrode curve derived from image logs of shale in the Cretaceous Qingshankou Formation, Gulong Sag, Songliao Basin (Well X). The first track is depth. The second track shows the full image log. The third track shows the static image log. The fourth track shows the corresponding dynamic image log. The fifth track displays the slab. The sixth track displays the button conductivity curve.

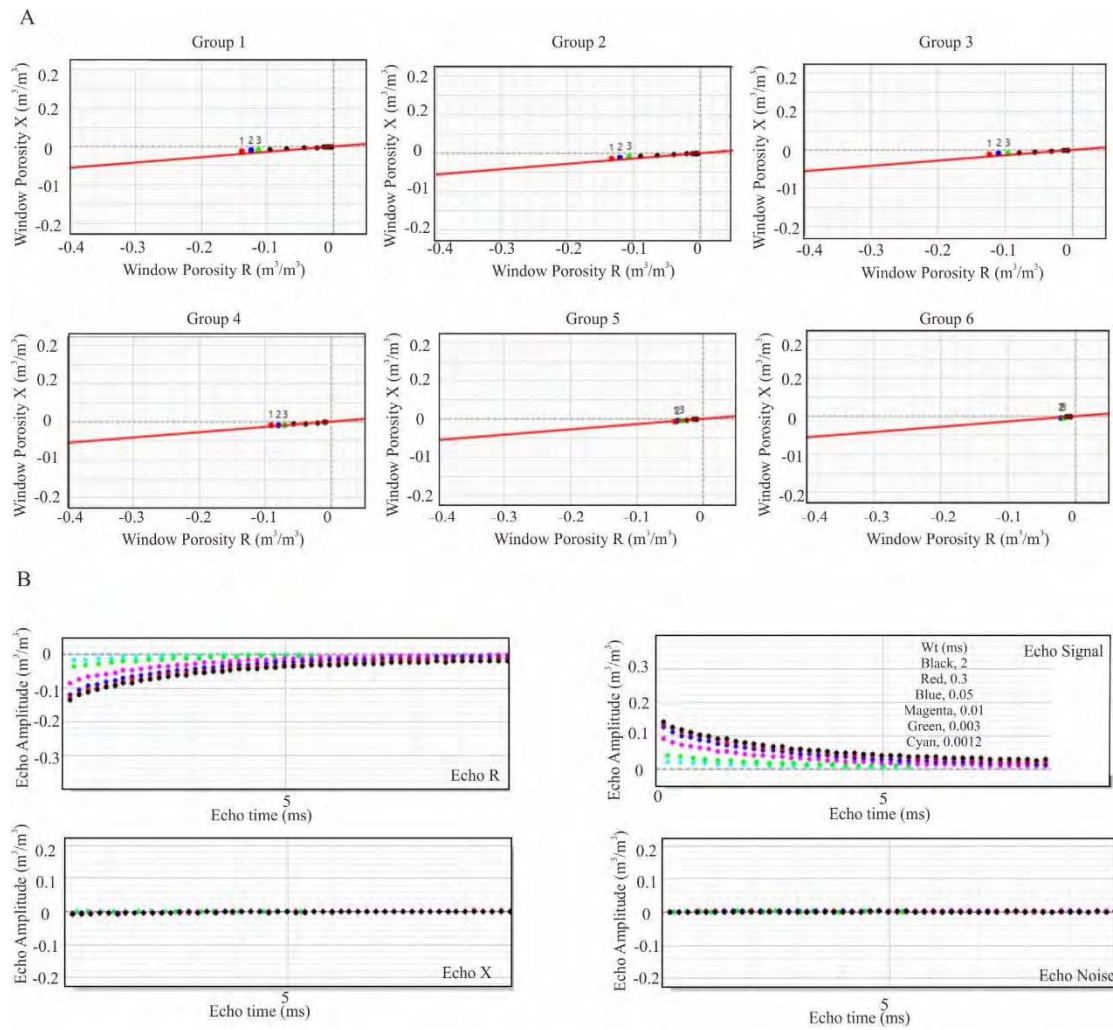


Figure 3. Reservoir quality control flag (Well Z), including Single phase quality control plot (A) and Echo quality control plot (B).

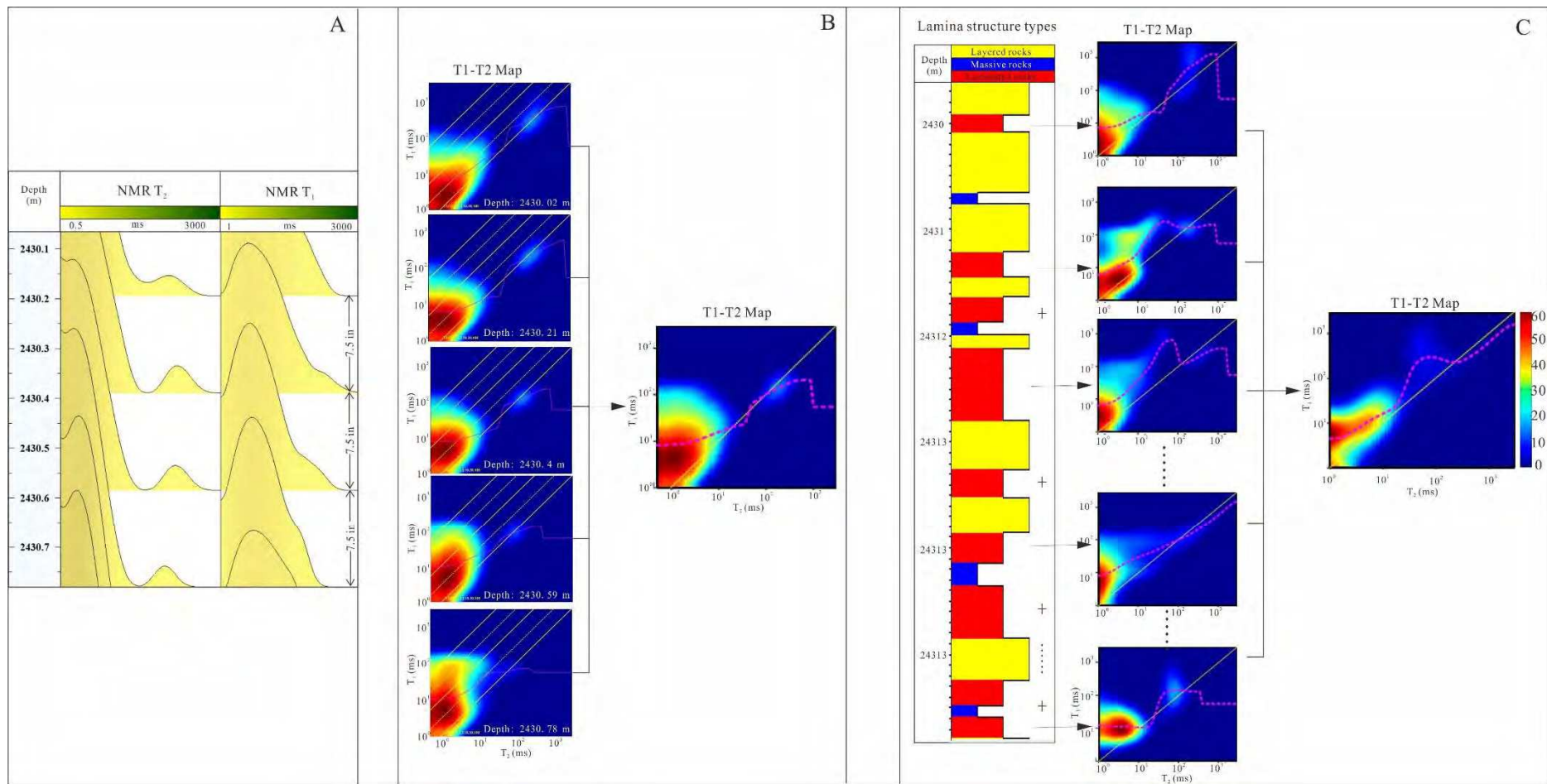


Figure 4. NMR T_1 and T_2 spectra (A), flowchart of T_1 - T_2 maps of stacked depth (B), and flowchart of T_1 - T_2 maps of stacked depth according to classification (C).

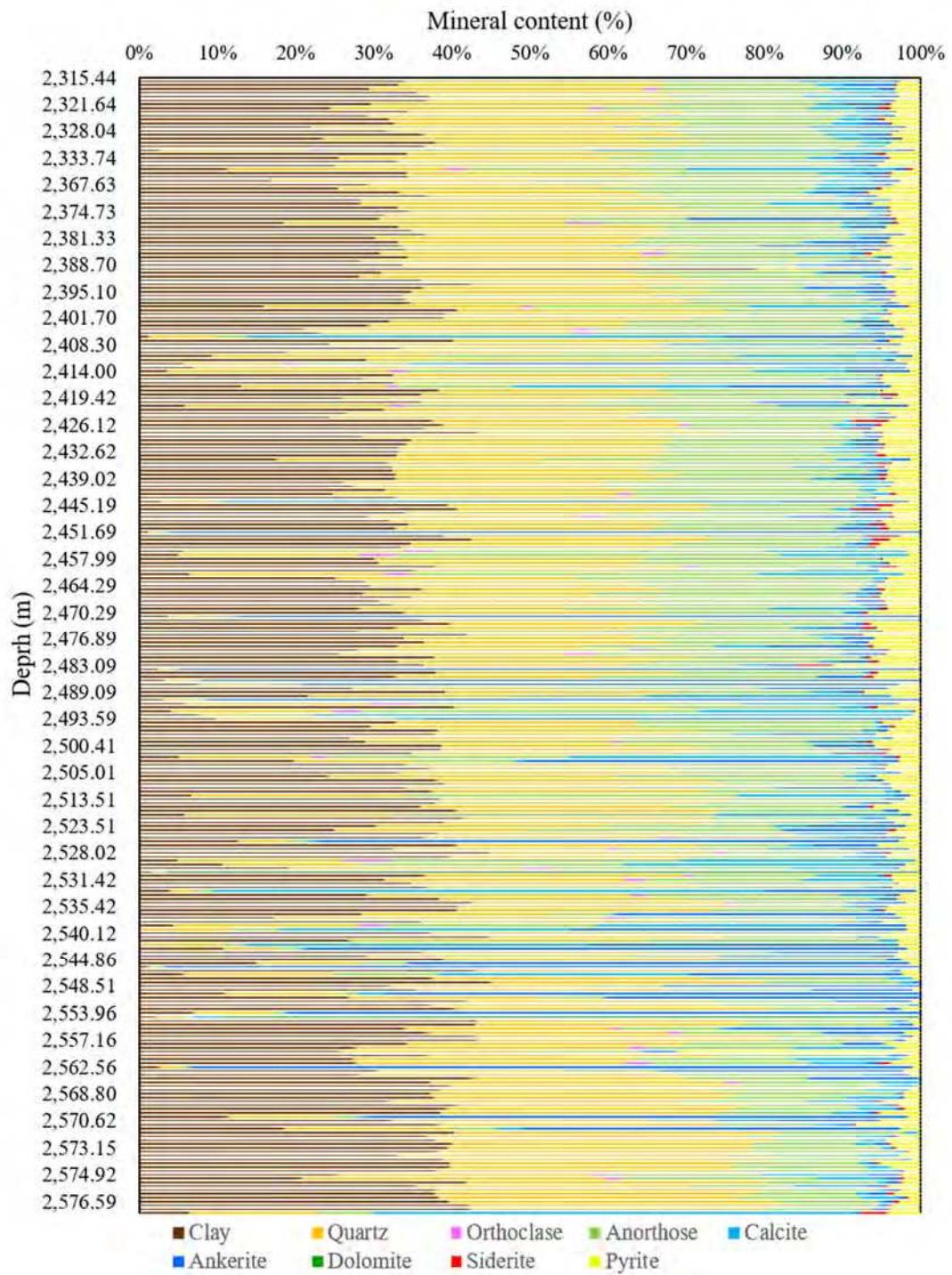


Figure 5. Results of XRD analyses showing the mineral composition of the shale oil reservoir.

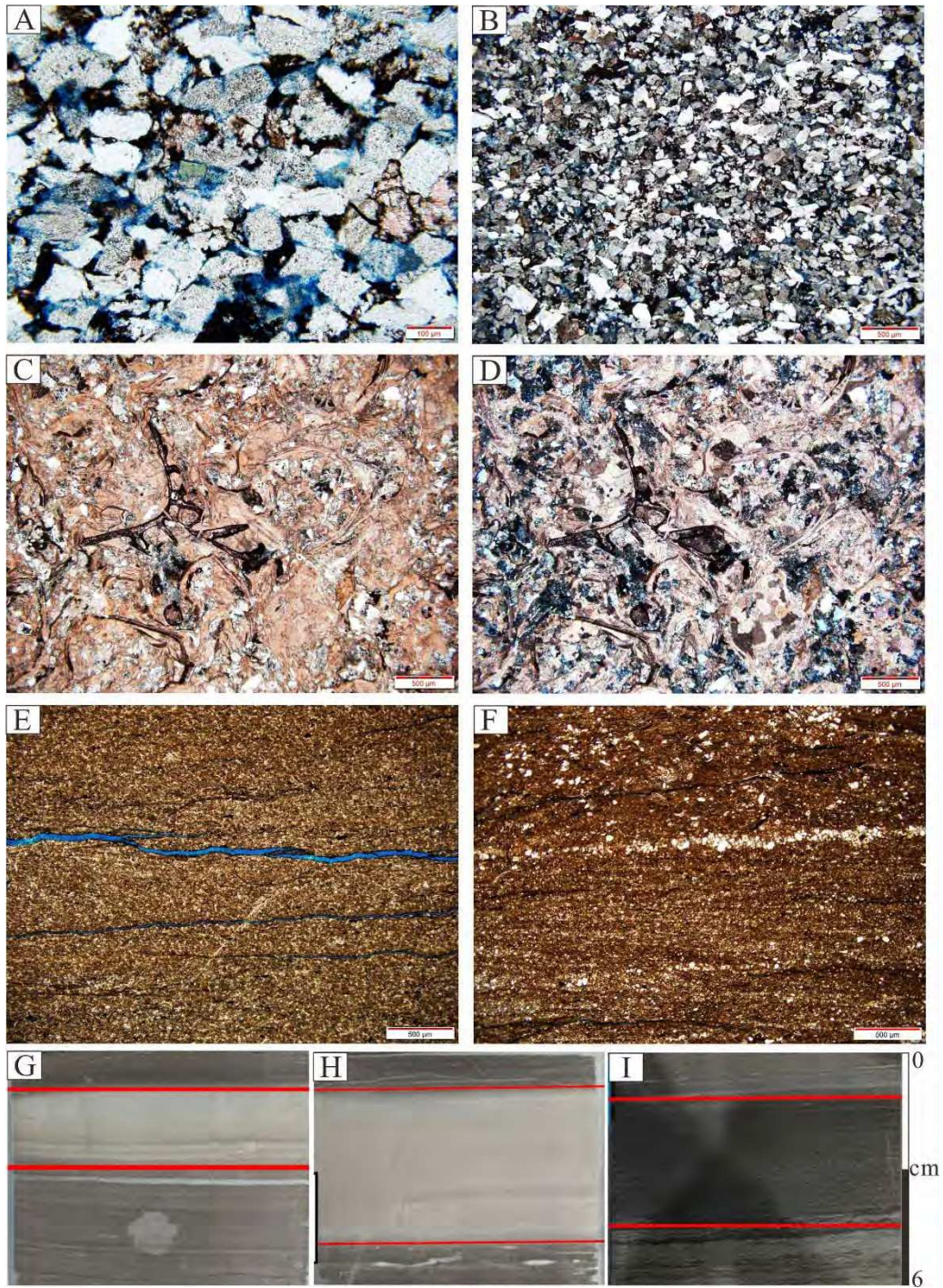


Figure 6. Thin sections and core photos showing examples of lithology in the Cretaceous Qingshankou Formation, Gulong Sag, Songliao Basin. A, B. Siltstone, Well A, 2374.88 m; C, D. Shell limestone, Well A, 2373.86 m; E, F. Shale, Well A, 2254.43 m; G. Dolostone, Well B, 2561.39 m; H. Dolostone, Well B, 2493.82 m; I. Mudstone, Well B, 2492.32 m.

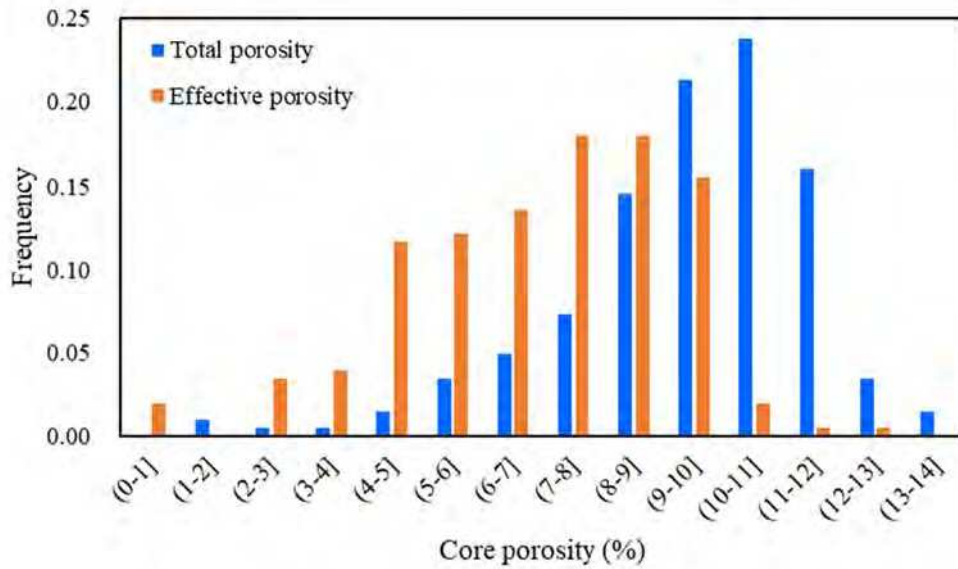


Figure 7. Frequency distribution of core porosity in the Qingshankou Formation, Gulong Sag, Songliao Basin (206 samples data of Well B).

Table 1. The classification standard of three types of lamina structure

Types of lamina structure	Laminated rocks	Layered rocks	Massive rocks
The thickness of each single layer (core observation)	Less than 0.01 m	Range from 0.01 m to 0.1 m	Larger than 0.1 m or no obvious layer
The density of layer (slab)	More than 100/m	Between 10/m and 100/m	No layers
Frequency of peaks and troughs (button conductivity curve)	More than 150/m	Between 20/m and 150/m	Less than 20/m

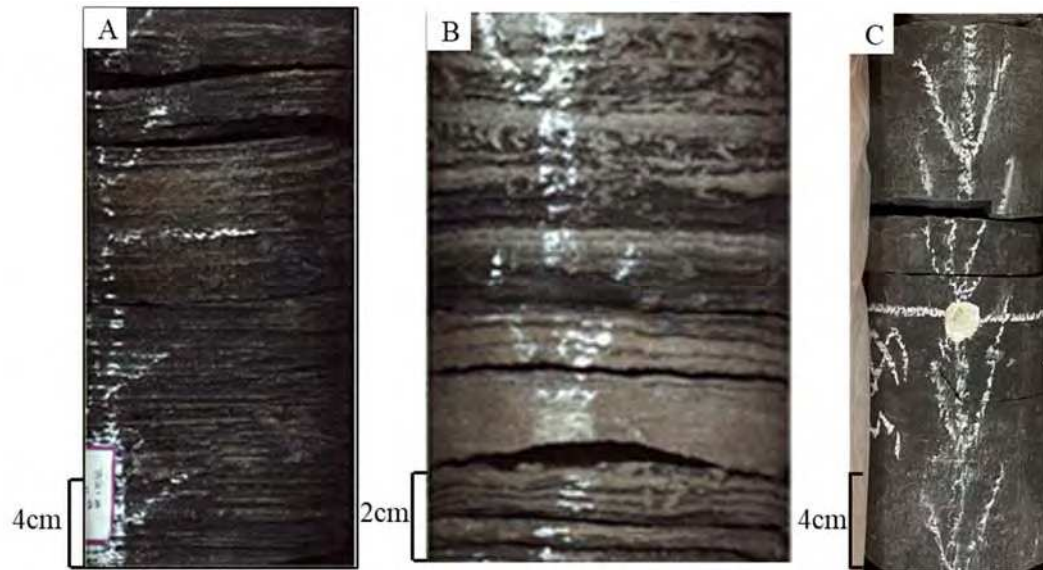


Figure 8. Core photos showing typical examples of lamina structure in the Cretaceous Qingshankou Formation, Gulong Sag, Songliao Basin. A. Laminated rocks in shale. B. Layered rocks in shale. C. Massive rocks in mudstone.

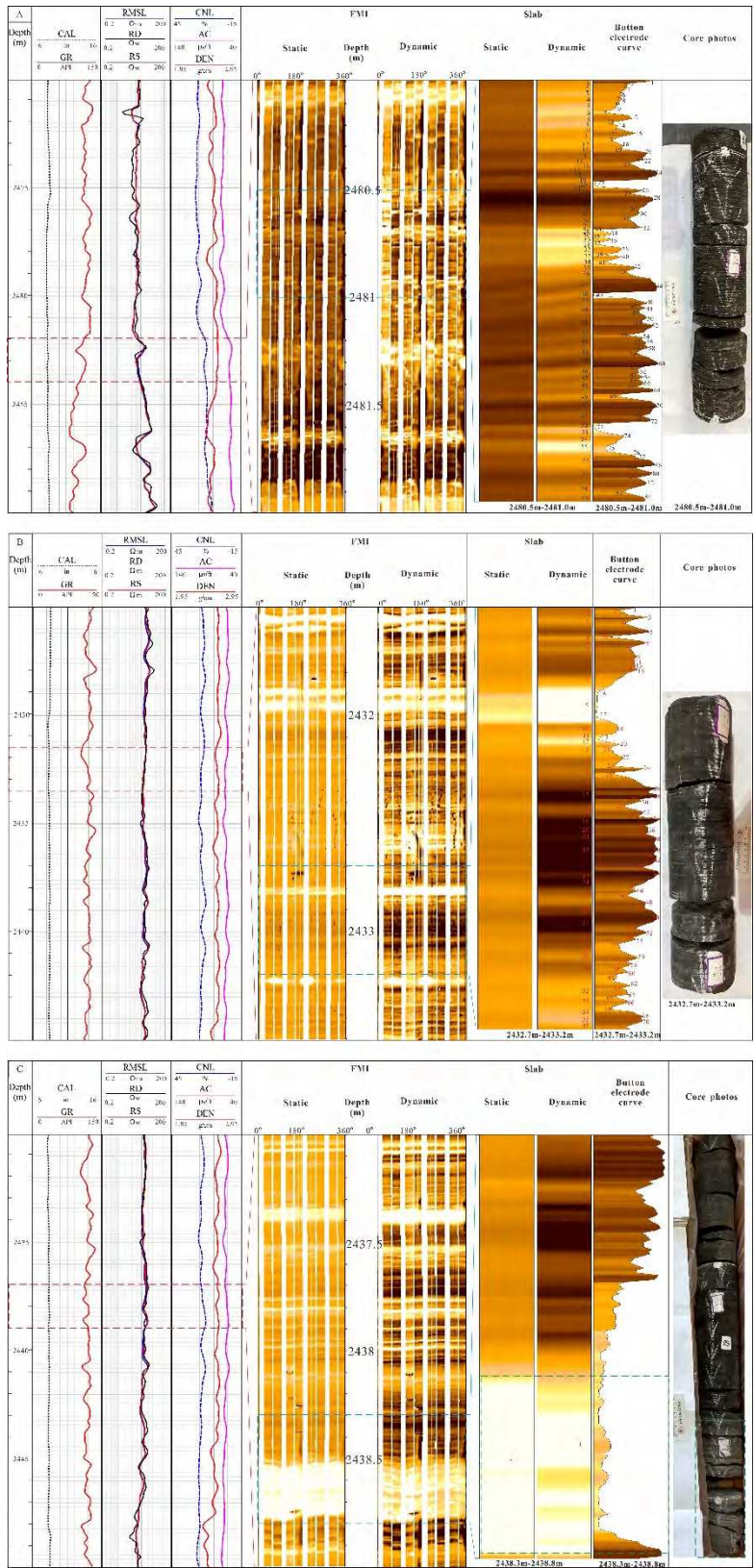


Figure 9. Well log response of three types of lamina structure in shale (well Y). A. Well log response of laminated rocks. B. Well log response of layered rocks. C. Well log response of massive rocks.

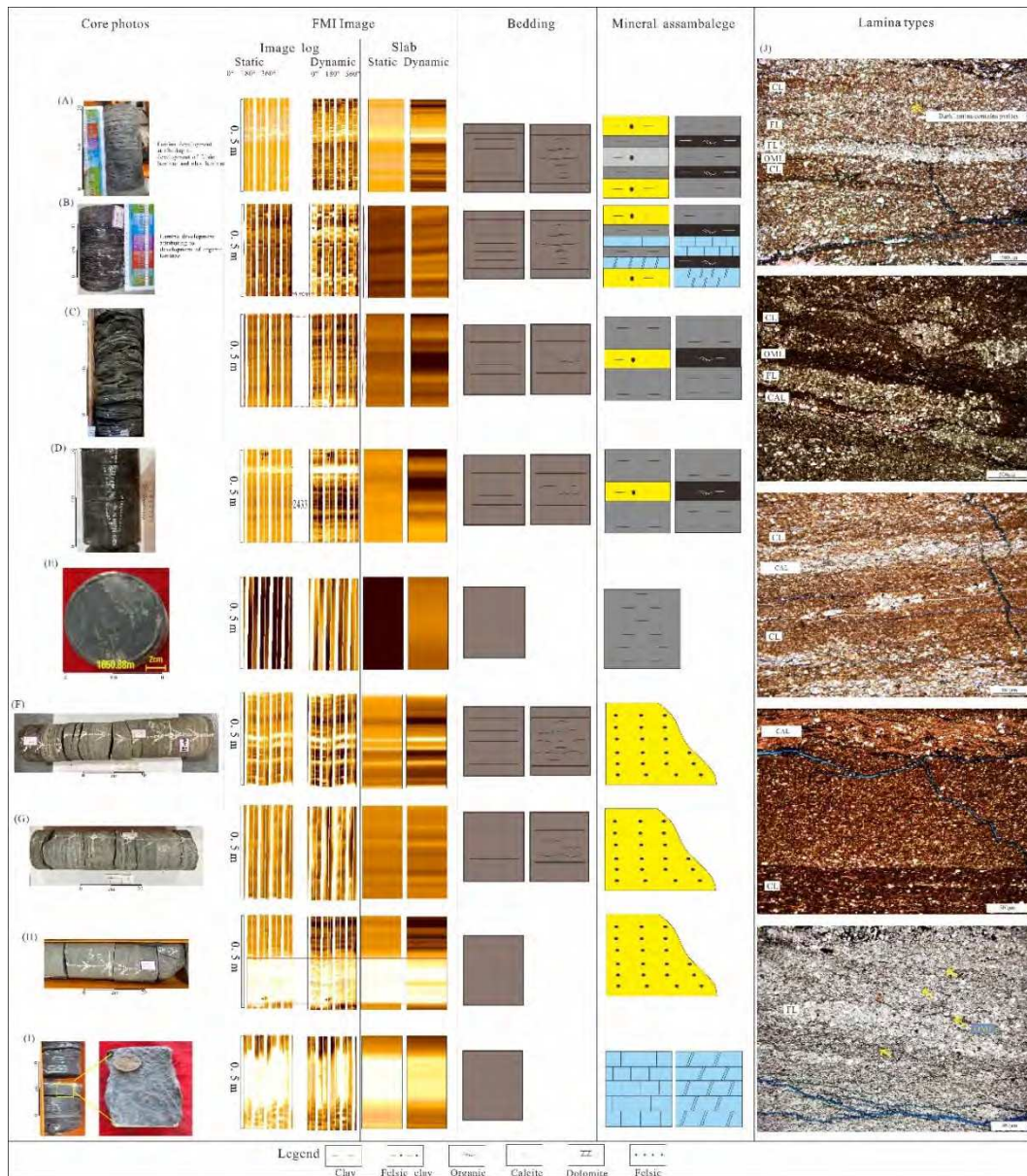


Figure 10. Lithology and lamina structure within shale of the Qingshankou Formation. Cores, wireline logs, thin sections, image logs, and button conductivity curves show examples of each lithology and their multi-scale lamina structure. Core photos, FMI images, slabs, and diagrams of lamina and mineral assemblages show example of each individual lithology. A. Laminated shale with felsic and clay laminae development. B. Laminated shale with organic and clay laminae development. C. Layered shale with bedding-parallel fractures developed. D. Layered shale. E. Massive mudstone. F. Laminated siltstone. G. Layered siltstones. H. Massive siltstone. I. Massive limestone. J. Various laminae types, including organic matter lamina (OML), felsic lamina (FL), clay lamina (CL), and carbonate lamina (CAL).

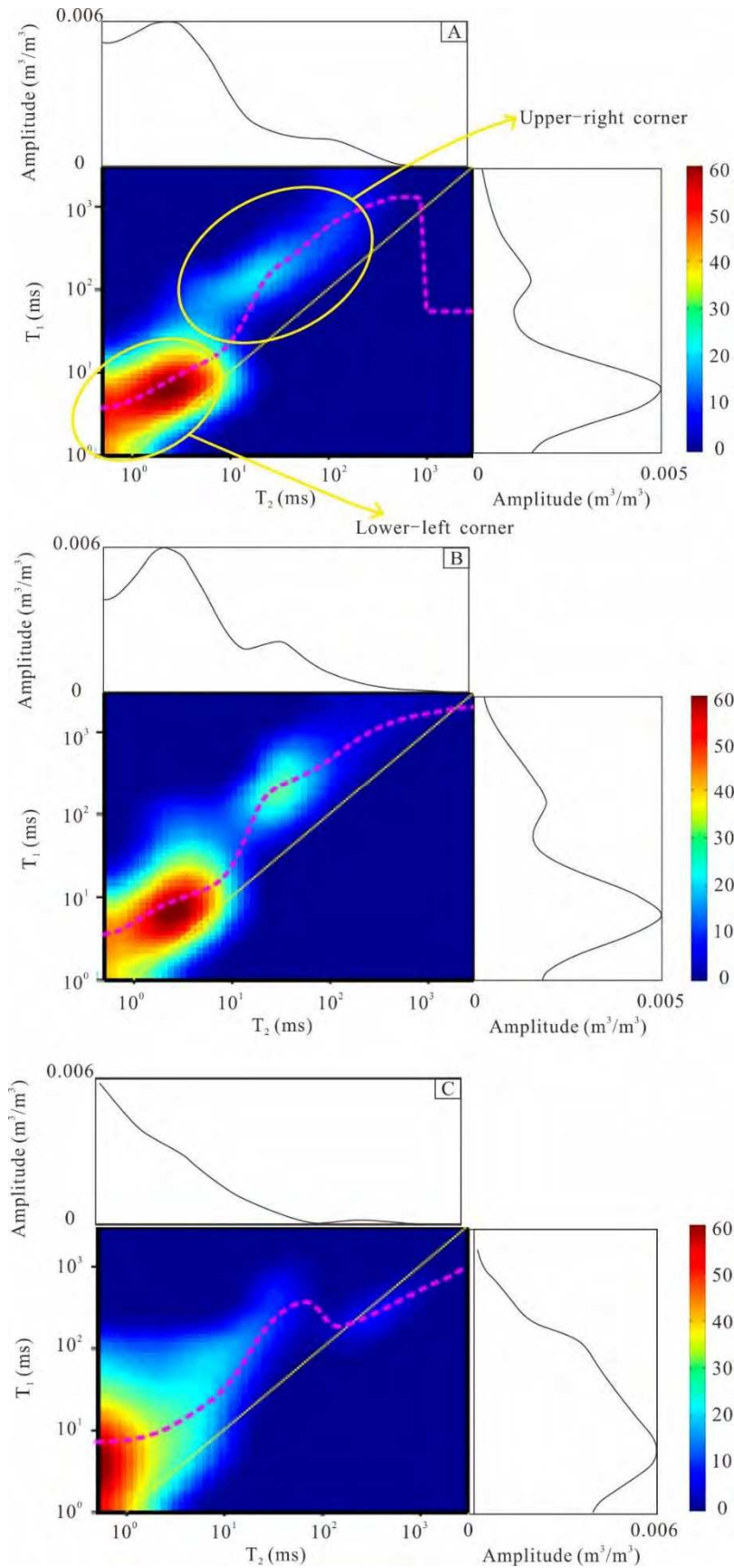


Figure 11. Three types T_1 - T_2 map corresponding to the three types of lamina structure in the Cretaceous Qingshankou Formation, Gulong Sag, Songliao Basin.

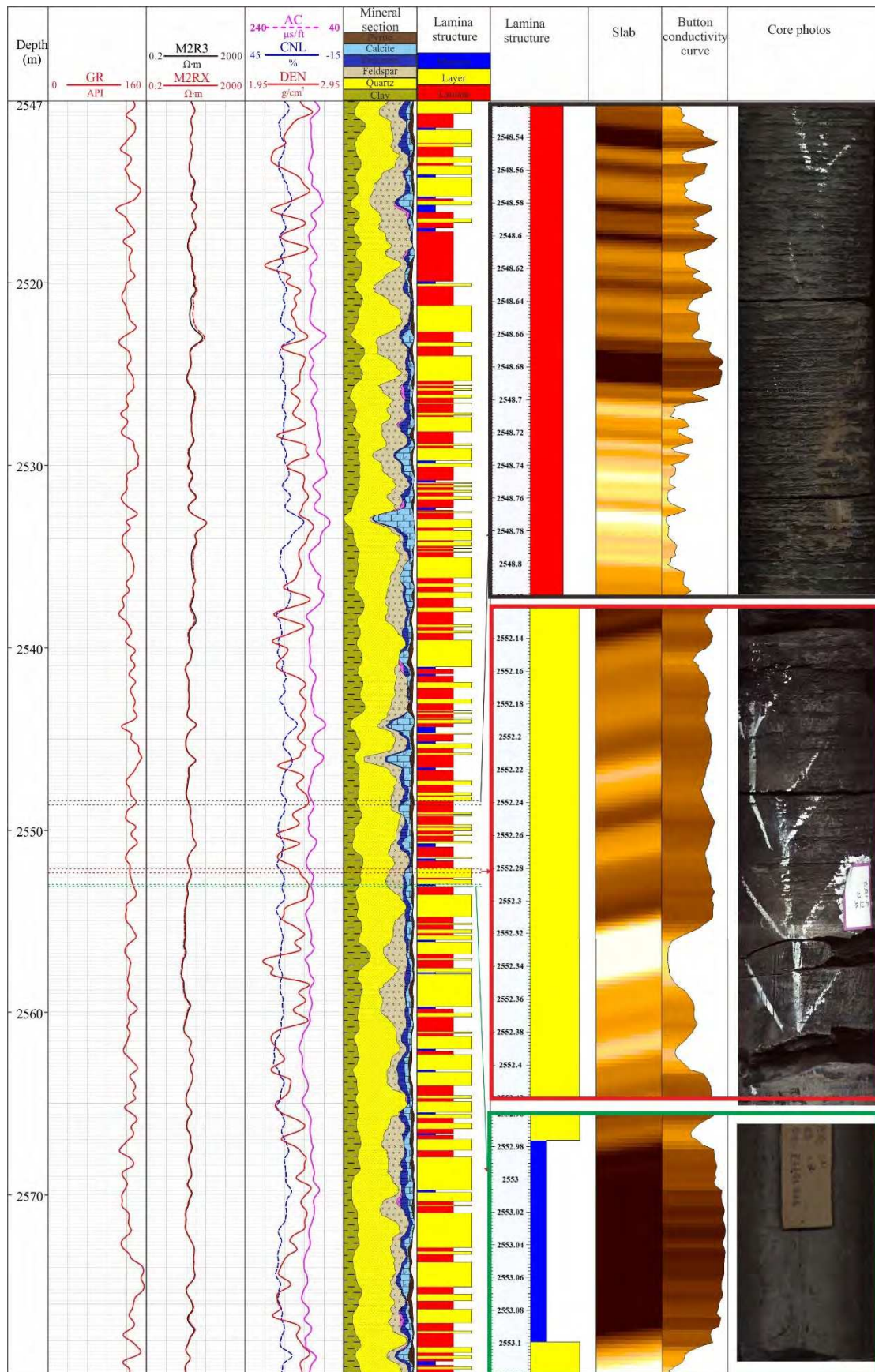


Figure 12. Lamina structure distribution in a single well in the Cretaceous Qingshankou Formation (well X). Tracks 7, 8, 9, and 10 are from strata at the same depth.

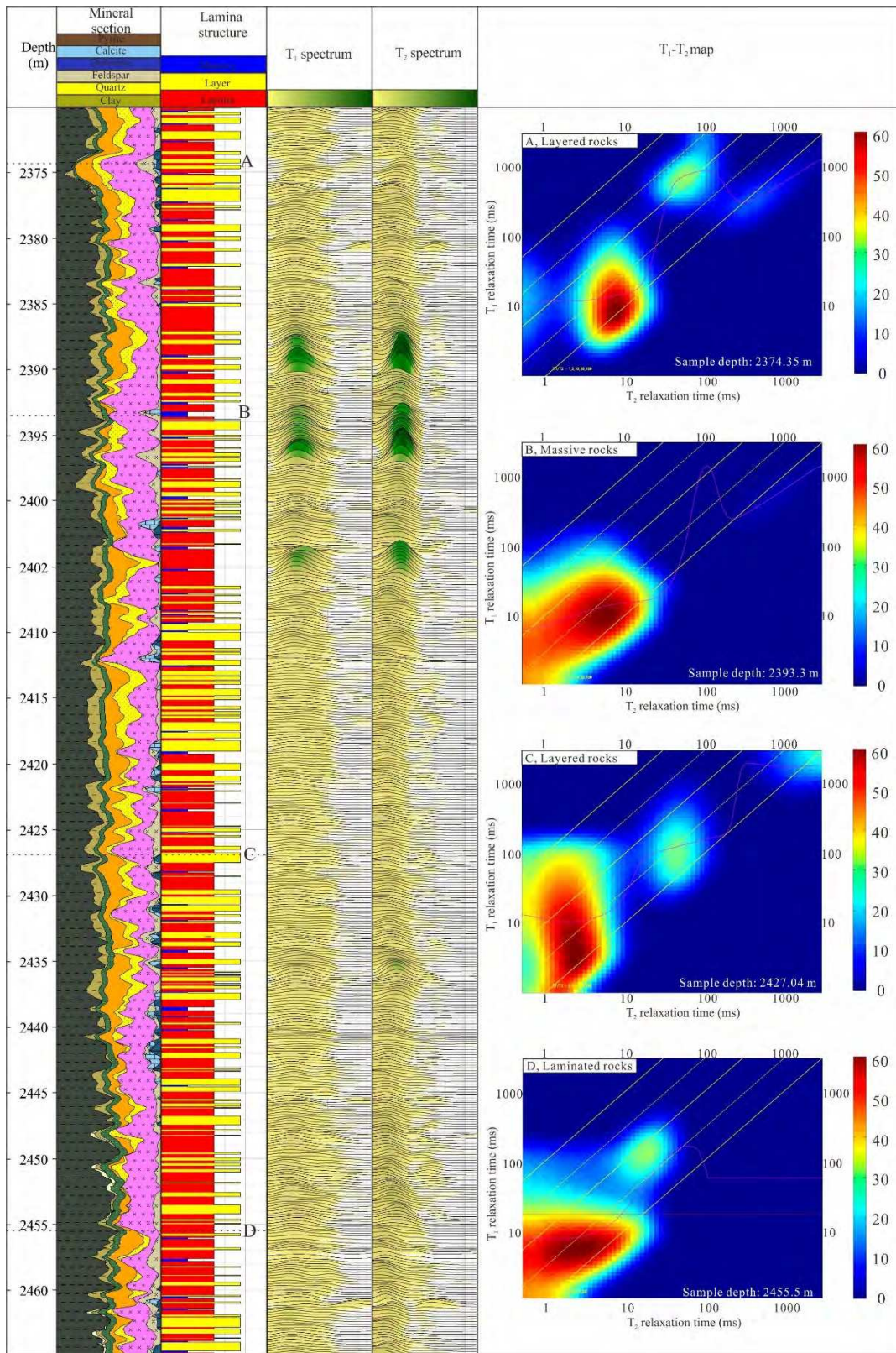


Figure 13. Relationships between lamina structure and reservoir quality and oil-bearing properties in shale in the Cretaceous Qingshankou Formation, Songliao Basin (well Y).

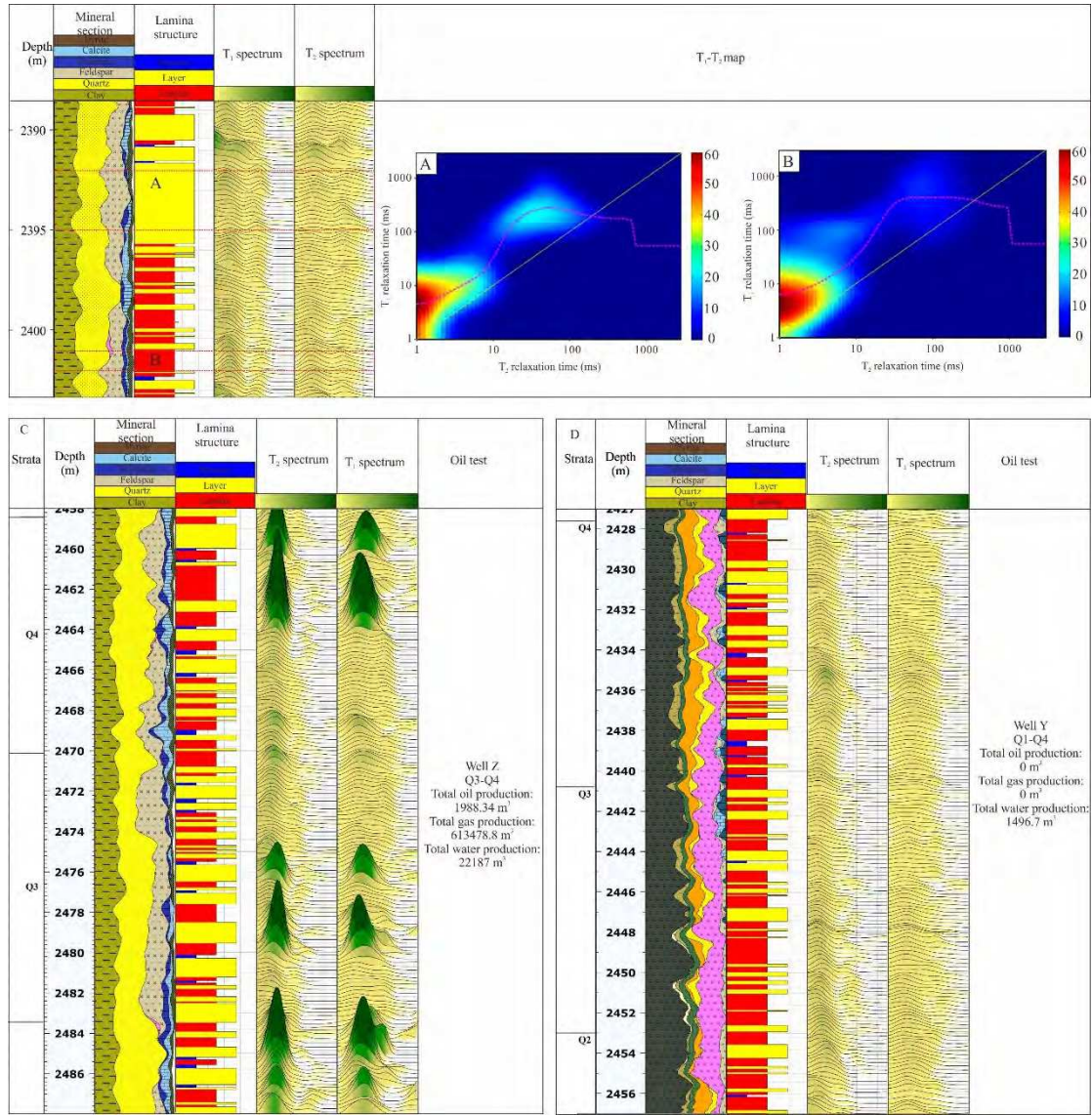


Figure 14. Relationships between laminae structure and reservoir quality and oil-bearing properties in shale in the Cretaceous Qingshankou Formation, Songliao Basin. Interval A (2392.0 m–2395.0 m) is layered rocks in well Z; interval B (2401.2 m–2402.0 m) is laminated rocks in well Z.

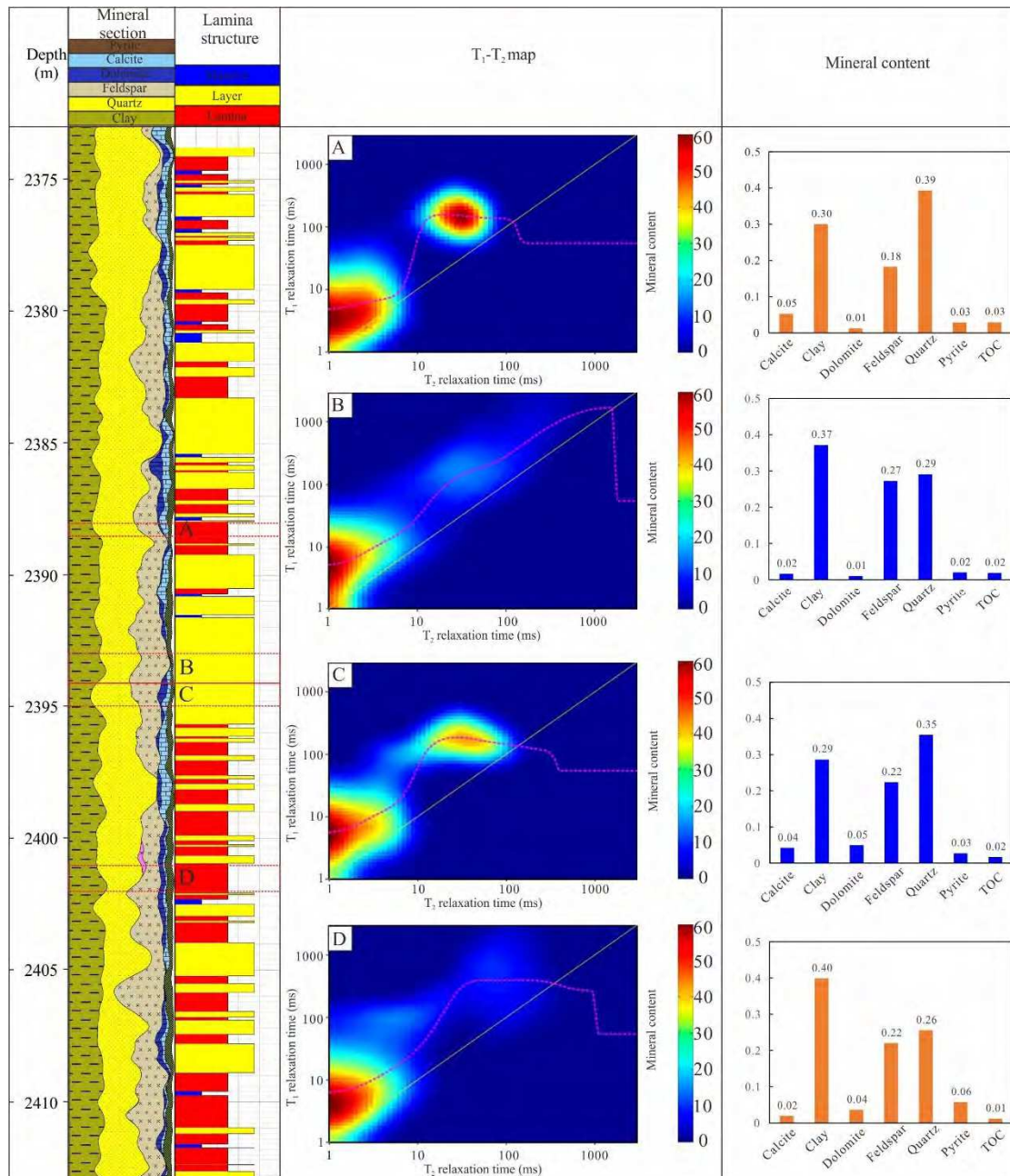


Figure 15. The effect of mineral content on the reservoir quality and oil-bearing properties in shale in the Cretaceous Qingshankou Formation, Songliao Basin (Well Z). A. laminated rocks. B. layered rocks. C. layered rocks. D. laminated rocks.